

Sediment Resuspension and Transport by Internal Solitary Waves

Leon Boegman¹ and Marek Stastna²

¹Environmental Fluid Dynamics Laboratory, Department of Civil Engineering, Queen's University, Kingston, Ontario K7L 3N6, Canada; email: boegmanl@queensu.ca

²Department of Applied Mathematics, University of Waterloo, Waterloo, Ontario N2L 3G1, Canada; email: mmstastna@uwaterloo.ca

Annu. Rev. Fluid Mech. 2019. 51:129–54

First published as a Review in Advance on August 15, 2018

The *Annual Review of Fluid Mechanics* is online at fluid.annualreviews.org

<https://doi.org/10.1146/annurev-fluid-122316-045049>

Copyright © 2019 by Annual Reviews.
All rights reserved

ANNUAL REVIEWS **CONNECT**

www.annualreviews.org

- Download figures
- Navigate cited references
- Keyword search
- Explore related articles
- Share via email or social media

Keywords

bottom boundary layer, internal waves, nepheloid layer, sand wave, sediment resuspension

Abstract

Large-amplitude internal waves induce currents and turbulence in the bottom boundary layer (BBL) and are thus a key driver of sediment movement on the continental margins. Observations of internal wave-induced sediment resuspension and transport cover significant portions of the world's oceans. Research on BBL instabilities, induced by internal waves, has identified several mechanisms by which the BBL is energized and sediment may be resuspended. Due to the complexity of the induced currents, process-oriented research using theory, direct numerical simulations, and laboratory experiments has played a vital role. However, experiments and simulations have inherent limitations as analogs for oceanic conditions due to disparities in Reynolds number and grid resolution, respectively. Parameterizations are needed for modeling resuspension from observed data and in larger-scale models, with the efficacy of parameterizations based on the quadratic stress largely determining the accuracy of present field-scale efforts.

1. INTRODUCTION

Internal solitary wave (ISW):

a finite-amplitude wave of permanent form in a stratified fluid; often computed by solving the Dubreil-Jacotin-Long equation, and described in the small-amplitude limit by the KdV equation

Fission:

transformation of an ISW into a wave train due to a change in the environmental conditions (e.g., total depth)

Bottom stress:

viscous (frictional) shearing force per unit of contact area applied by the fluid to the sediment water interface; also known as bed stress

Internal solitary waves (ISWs), or waves of permanent form that occur in the interior of natural bodies of water due to differences in density between adjacent layers of water (stratification), are common features of lakes (e.g., Boegman et al. 2003, Farmer 1978, Thorpe 1971), estuaries (e.g., Bourgault et al. 2014, Nash & Moum 2005, Richards et al. 2013) and the coastal ocean (e.g., Bogucki et al. 1997, Jackson 2007, Klymak & Moum 2003). ISWs have speeds of propagation that are larger than the linear longwave speed, which is the maximum propagation speed of small-amplitude waves. Typically, ISWs have a bell-like horizontal structure and a vertical structure that displaces surfaces of constant density either purely downward (waves of depression) or purely upward (waves of elevation) from their rest height. Through analysis of satellite images, Jackson (2007) identified ISW packets along nearly every coastline worldwide on 95% of observation days (**Figure 1**). With wavelengths of $\sim 0.1\text{--}1$ km, amplitudes of $\sim 10\text{--}100$ m, and currents of $\sim 0.1\text{--}1$ m/s, ISWs are characteristically smaller in lakes than oceans. They transport significant energy from their oceanic generation sites (e.g., ~ 3 GJ/m) (Huang et al. 2016) with a large associated energy flux (e.g., ~ 8.5 kW/m) (Chang et al. 2006). In lakes, ISWs may contain as much as 10–15% of the available potential energy introduced by the surface wind stress (Boegman et al. 2005b) or $\sim 1\%$ of the internal Kelvin wave energy (Boegman et al. 2003). ISWs are typically shoreward-propagating, although offshore-propagating (Carter et al. 2005, Rayson et al. 2011), oblique along-shelf (Quaresma et al. 2007), and standing ISW-type waves (Rayson et al. 2012) have been observed. As the waves break (e.g., Barad & Fringer 2010, Fructus et al. 2009) and shoal (e.g., Orr & Mignerey 2003, Shroyer et al. 2009), wave energy is lost to dissipation (e.g., $10^{-7}\text{--}10^{-6}$ W/kg) (Lien 2005) and turbulent mixing (e.g., $\sim 10^{-2}$ m²/s) (Moum et al. 2003), thus influencing lake/ocean circulation, biogeochemical cycling, and sediment dynamics (e.g., Haury et al. 1979, Scotti & Pineda 2007, Wang et al. 2007). For example, the occurrence of several large wave-shoaling events per tidal cycle is believed to be sufficient to supply the required nutrients to the euphotic zone on the Scotian Shelf (Helfrich 1992, Sandstrom & Elliott 1984). Shoaling of ISWs is not necessarily violent, and for gentle slopes, there is the possibility that a single wave will fission into several ISWs or a wave train.

ISWs induce bottom stress, which may become sufficient to initiate sediment movement, and near-bed instability can resuspend sediments. For large-amplitude waves over flat bottoms (e.g.,

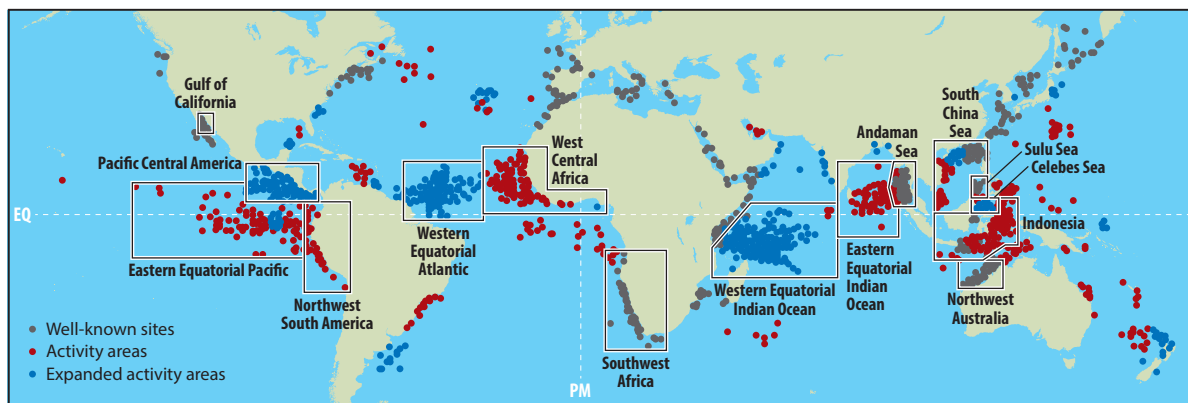


Figure 1

Global distribution of internal solitary waves. Internal waves observed from August 2002 through May 2004. Shown are well-known occurrence sites (gray), new areas of activity (red), and areas of geographically expanded activity (blue). Figure adapted from Jackson (2007), with permission from Wiley.

CLASSIFICATION OF ISW BREAKING REGIMES

Similar to the classification of surface wave breakers, Boegman et al. (2005a) analyzed experimental data to classify the breaking of shoaling ISWs in terms of the bed slope (s) and ISW slope (amplitude, a , divided by wavelength, λ) using an internal form of the Iribarren number:

$$Ir = \frac{s}{\sqrt{a/\lambda}}.$$

There is a qualitative change from plunging to collapsing to surging as Ir increases: Plunging breakers have an overturning leeward face, which becomes gravitationally unstable; collapsing breakers are similar to plunging, except that separated flow pushes the leeward face backward upon itself; and surging breakers reflect with little mixing.

The critical Ir distinguishing the transition between breaker classifications depends on the particular definition of a and λ (Sutherland et al. 2013), but in general, plunging breakers form for $Ir < \sim 0.7$, collapsing breakers form for $0.7 < Ir < 1$, and surging breakers form for $Ir > 1.5$ (Boegman et al. 2005a, Sutherland et al. 2013). From numerical simulations, Aghsaei et al. (2010) classified ISW breakers in s versus a/λ space, and K. Nakayama, T. Sato, K. Shimizu, and L. Boegman (submitted manuscript) proposed an improved delineation between collapsing and plunging breakers by scaling $s/(a/\lambda)$ with a wave Reynolds number. For ISWs shoaling on gentle slopes ($s < \sim 0.01$), fission followed by bolus formation is expected (Aghsaei et al. 2010, Moum 2012).

Aghsaei & Boegman 2015, Stastna & Lamb 2008) and ISWs incident on steep slopes (collapsing and plunging breakers; see the sidebar titled Classification of ISW Breaking Regimes) (Boegman et al. 2005a), flow separation may occur in the adverse pressure gradient wake region behind the waves, driving strong turbulent burst events (**Figure 2**) with maximum vertical velocities of ~ 0.1 m/s and enhanced sediment resuspension of ~ 100 g/m² per day (Hosegood & Van Haren 2004, Hosegood et al. 2004). Here, resuspension is defined as the uplifting of sediment particles by water currents (often by turbulence) to occupy the main water column. Smaller waves on gradual slopes will form waves of elevation and bulges (e.g., Helffrich 1992, Sutherland et al. 2013) with instability and resuspension at the wave front (e.g., Moum et al. 2007, Richards et al. 2013). Near-bed instability is, therefore, believed to be the principal mechanism driving ISW-induced sediment resuspension in coastal regions.

Sediments can be redistributed by ISWs through both bed load transport and resuspension. They are pumped vertically through the water column (e.g., Bogucki et al. 1997, Valipour et al. 2017) until background stratification inhibits vertical transport, and then they intrude laterally in the form of nepheloid layers (**Figures 3 and 4**) and form geologic features (**Figure 5**) such as sand waves (e.g., Reeder et al. 2011). Internal wave shoaling and internal tides are believed to affect sedimentation patterns (Pomar et al. 2012) and bottom gradients (Cacchione et al. 2002), thereby shaping the continental slope and its geological history.

Below, we review field observations of sediment resuspension and transport by ISWs (Section 2) and theoretical, numerical, and experimental results on both the laboratory and field scale (Section 3) that identify mechanisms leading to sediment resuspension and transport, as well as the parameterizations of these. Section 4 provides an outlook on future research on these subjects.

2. OBSERVATIONS OF ISW-INDUCED SEDIMENT RESUSPENSION AND TRANSPORT

The satellite observations by Jackson (2007, table 1), while not globally uniform, categorized 15 major geographic regions of intense ISW activity. 76% of his observed occurrences are located

Adverse pressure gradient: a pressure gradient acting to decelerate fluid; in the bottom boundary layer, this can lead to flow separation and vortex formation

Bolus: a wave with an unsteady trapped core propagating along the bottom, often detached from the pycnocline; it can contain fluid denser than the ambient fluid

Bed load: particles in a flowing fluid that are transported along the bottom (or bed)

Nepheloid layer: from the Greek “nephos,” or “cloud,” a layer of water in the deeper portion of the water column containing significant suspended sediment

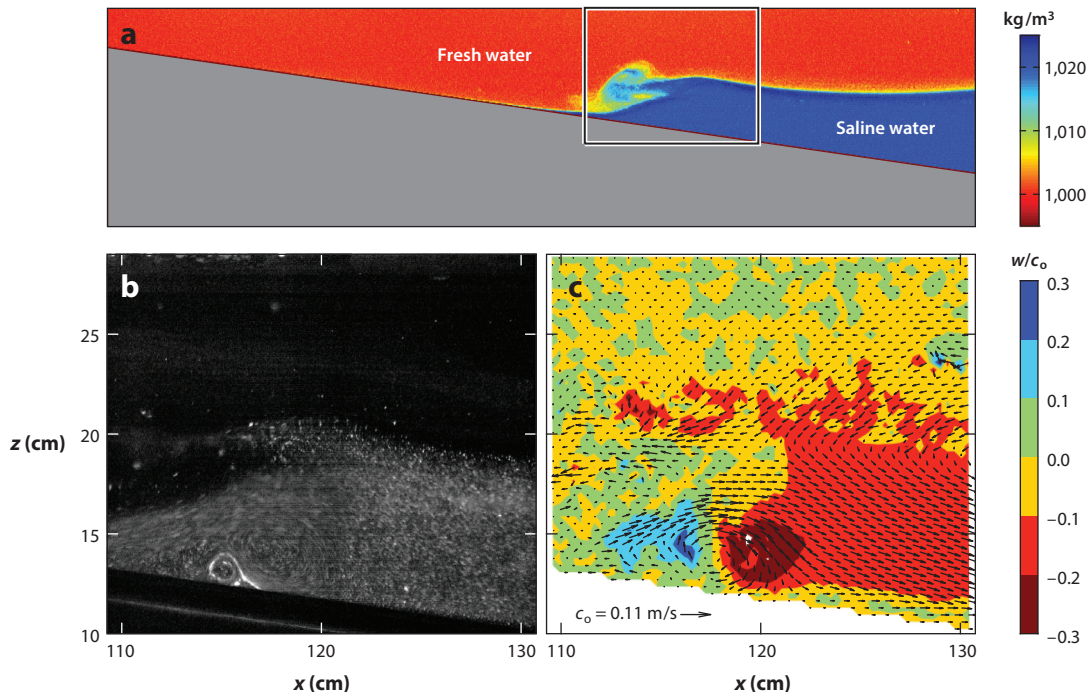


Figure 2

Experiments showing resuspension from an internal solitary wave (ISW) shoaling from right to left. (a) False-color images of measured density field during shoaling of an ISW packet in tilting tank experiments. The upper (red) layer is fresh water and the lower (blue) layer is saline, with densities given in kg/m^3 . (b) Raw image of neutrally buoyant seed particles in the square subregion shown in panel a. (c) Velocity vectors and instantaneous vertical velocity, normalized by the linear wave speed, w/c_o , computed from panel b using particle image velocimetry. The arrow shown on the slope denotes the linear phase speed, $c_o = 0.11 \text{ m/s}$. A near-bed vortex was observed to enhance the local Reynolds stress and resuspend a high concentration of seed particles from the bed (as shown in panel b). Figure generated using data from Boegman & Ivey (2009). For an animation of this experiment, the reader is referred to **Supplemental Videos 1–4**.

Supplemental Material >

in these regions. While ISWs have been intensively studied in many of these regions (reviewed in Helffrich & Melville 2006 and Lamb 2014), research on observed ISW-induced resuspension and transport remains limited.

We group observations of sediment resuspension by ISWs into four geographic regions (Section 2.1), only one of which (South China Sea) is among the top 15 ISW-active regions categorized by Jackson (2007). The remaining three sites are close to oceanographic institutes, suggesting present research on ISW-induced resuspension is governed by opportunity and convenience, leaving many potential resuspension sites underinvestigated. We group observations of sediment transport by ISWs into five geographic regions (Section 2.2), two of which (South China Sea and Northwest Australia) are among the top 15 ISW-active regions categorized by Jackson (2007). ISW-induced sediment transport is identified by the presence of large-scale subaqueous dunes, or sand waves, at depths sufficient to allow the potential role of surface waves to be neglected. Observations of marine sand waves in isolation abound (Hulscher & Dohmen-Janssen 2005); the focus here is on studies in which the morphological development is directly attributed to ISW forcing. The related issue of sediment transport by gravity currents has been reviewed by Meiburg & Kneller (2010).

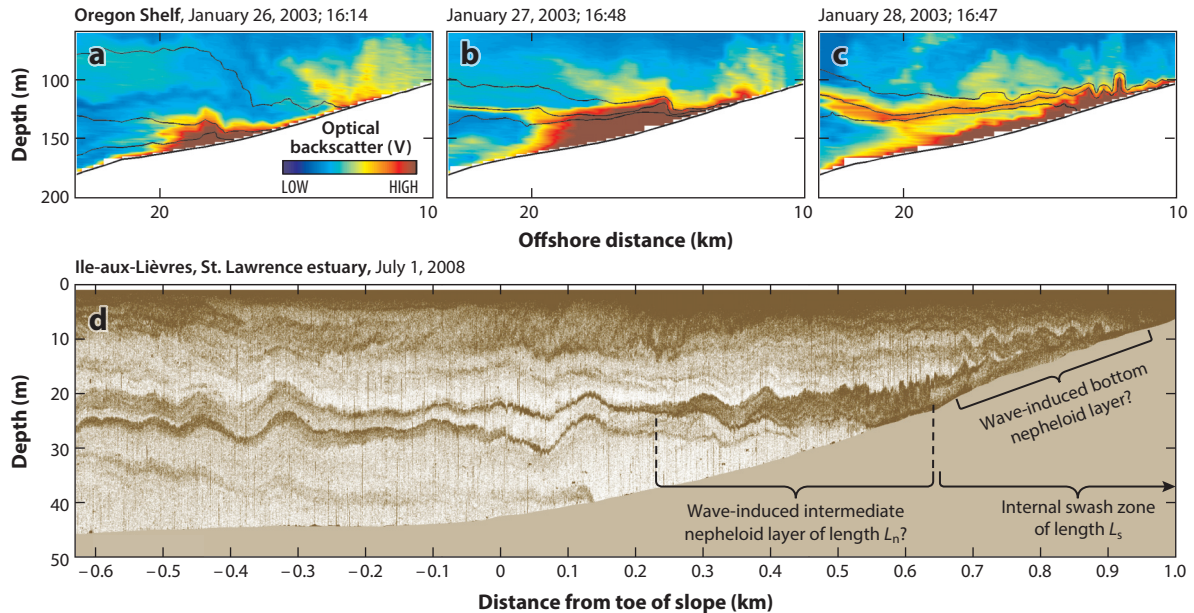


Figure 3

Shoaling internal solitary wave (ISW) fronts and resultant nepheloid layers. (a–c) Cross-shelf structure of shoaling fronts and ISW packets on three successive days in January 2003 on the Oregon shelf. Isopycnals (black lines) are spaced at 0.5 kg/m, and the background color denotes optical backscatter. The upper 50 m of the water column has been omitted. (d) Echogram suggesting sediment transport by shoaling ISWs along the flank of Ile-aux-Lievres, an island in the St. Lawrence River estuary. Both the bottom and intermediate nepheloid layers are indicated as well as the remnant of a shoaling ISW (see Figure 4). Panels a–c adapted from Moum et al. (2007), with permission from the American Meteorological Society, and panel d adapted from Bourgault et al. (2014), with permission from Elsevier.

2.1. Sediment Resuspension by ISWs

Published observations of sediment resuspension by ISWs may be grouped into four geographic regions. These include the United States Pacific Coast, the North American Atlantic Coast, the European North Atlantic Coast and the South China Sea. The observations from each of these regions are reviewed below.

2.1.1. United States Pacific Coast. In a strongly stratified bottom boundary layer (BBL) on the California shelf, Bogucki et al. (1997) observed an increased concentration of particulates in the water column to accompany the passage of ISW packets. Resuspension coincided with periods of low bed stress (from the quadratic stress law), suggesting pumping of sediment into the water column in the flow separation region. On the shelf, off Oceanside, California, Johnson et al. (2001) observed spikes in suspended particles at the trailing edges of ISWs of depression. Each trailing edge had a bore-like face with strong convergent bottom currents that were not correlated with high bottom stress. Over Oregon's continental shelf, Klymak & Moum (2003) observed shoaling ISWs with highly turbulent trapped cores and enhanced optical backscatter. The observed turbulence was not sufficient to completely dissipate wave energy before reaching shore, suggesting that the ISWs terminate abruptly farther up-shelf, implying enhanced cross-shelf transport. Further investigation (Moum et al. 2007) showed the ISWs at the head of sharp, near-bottom density fronts, with high optical backscatter near the bed and at the

Bottom boundary layer (BBL): the layer (possibly turbulent) near the bottom where horizontal currents are rapidly reduced to zero by the no-slip bottom boundary condition

Quadratic stress law: a phenomenological estimate of the bottom shear stress as proportional to the square of the velocity at a fixed height above the bottom

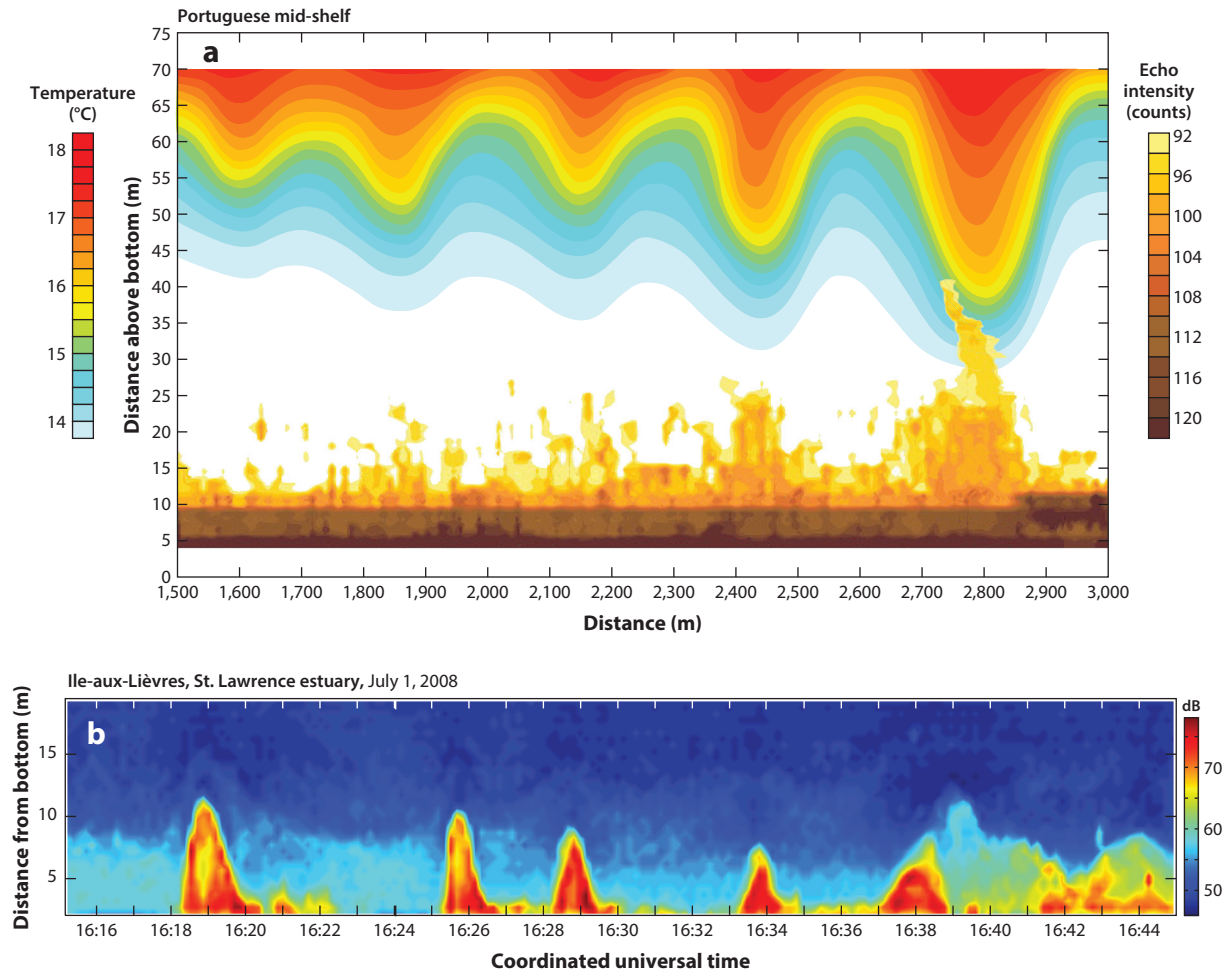


Figure 4

Characteristic observations of acoustic backscatter showing resuspension associated with shoaling internal solitary waves (ISWs) of elevation and depression. (a) Overlay of temperature profile and echo intensity, showing resuspension during the passage of a packet of ISWs of depression on the Portuguese mid-shelf. (b) Acoustic backscatter during shoaling of a packet of ISWs of elevation along the flank of Ile-aux-Lièvres, an island in the St. Lawrence River estuary (see Figure 3b). Panel a adapted from Quaresma et al. (2007), with permission from Elsevier, and panel b adapted from Richards et al. (2013), with permission from Wiley.

leading edges (Figure 3a–c), indicating sediment resuspension, likely by elevated turbulence ($>10^{-7} \text{ W/kg}$). On the Monterey Bay shelf, Carter et al. (2005) observed downslope-propagating ISWs that transformed into waves of depression at the canyon rim, with the most intense acoustic backscatter at the leading edge and lower backscatter within the core. Internal wave-induced resuspension over the outer shelf was found to provide material that is sustained on shelf mud belts (Cheriton et al. 2014a), although the presence of suspended particulates was not correlated with local bed stress. Recent observations from a multi-institution field experiment on ISW propagation, transformation, and dissipation, from the mid-continental shelf through the inner shelf and into the surf zone near Point Sal (California), are presently under analysis (Barth et al. 2018).

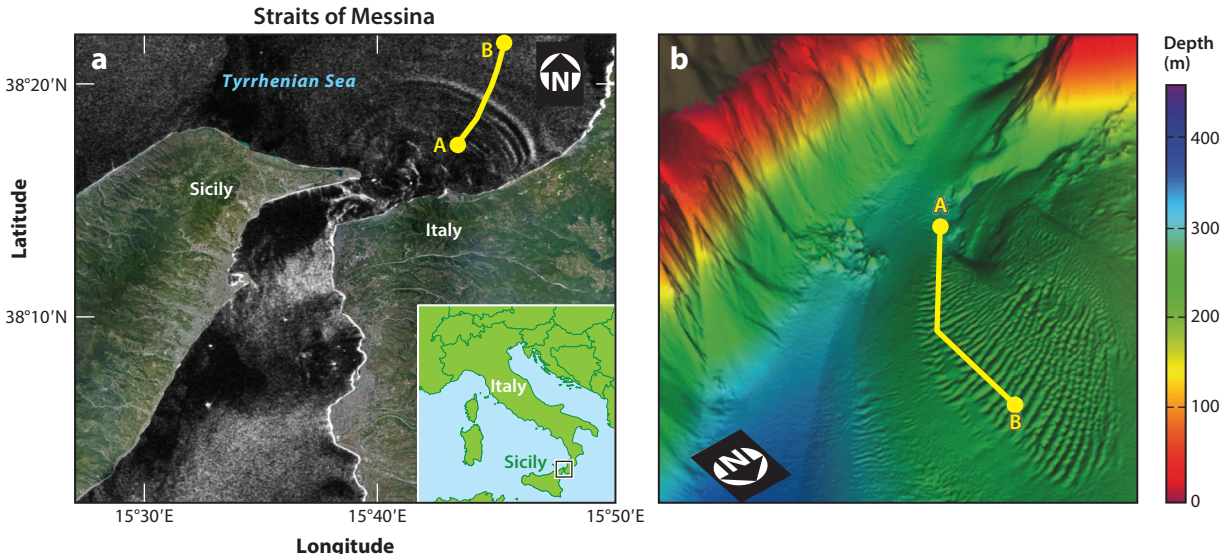


Figure 5

Internal solitary waves (ISWs) and associated sand waves. (a) Satellite image showing surface manifestations of ISW packets propagating northward into the Tyrrhenian Sea. (b) Bathymetric map showing the sand wave field. The yellow line in panel *a* indicates the transect in panel *b*. Figure adapted from Droghei et al. (2016) under the Creative Commons CC-BY license.

2.1.2. North American Atlantic Coast. Near-bottom high-frequency ISWs of elevation were observed in Massachusetts Bay (Scotti & Pineda 2004), with elevated turbulence ahead of the waves and unusually large acoustic backscatter. On the Mud Patch of the Middle Atlantic Bight, both mode-1 and mode-2 waves were observed to resuspend sediment under stormy and calm conditions (Bogucki et al. 2005). Large-amplitude ISWs resuspended sediments in Massachusetts Bay (Butman et al. 2006) when currents exceeded ~ 0.2 m/s at 1 m above the bottom in each tidal cycle during late August for a total of 0.4 days each summer. In the St. Lawrence River estuary, echograms suggest shoaling ISWs create upslope sediment transport within boluses (Figure 4*b*) and ~ 10 -m-thick, wave-induced bottom and intermediate nepheloid layers (Bourgault et al. 2014, Richards et al. 2013) (Figure 3*d*).

2.1.3. European North Atlantic Coast. In the middle of the Faeroe–Shetland channel (Hosegood et al. 2004, Hosegood & Van Haren 2004) and the base of the Rockall continental slope (Bonnin et al. 2006), solibore shoaling completely dominated resuspension events. Mid-slope sediment fluxes were $\mathcal{O}(10^2)$ larger than background values, while resuspended material at the slope base was laterally advected over short distances. In contrast to the observations of Bogucki et al. (1997), solibore resuspension occurred during abrupt bursts of high bed stress associated with a rotor at the leading edge (Thorpe 1998), creating strong near-bed vertical velocities. Over the northern mid-shelf of Portugal, Quaresma et al. (2007) showed the propagation of large-amplitude ISWs forcing strong bottom current pulses (Figure 4*a*). Turbidity profiles and acoustic backscatter suggested sediment remobilization. The ISW-induced bottom stress caused the Shields parameter to exceed critical levels for both sediment mobility and resuspension.

2.1.4. South China Sea. Extremely large ISWs were routinely observed in the South China Sea (e.g., 240-m amplitude, 2.55 m/s currents; Huang et al. 2016), and where these waves shoal,

sediment resuspension was expected. Reeder et al. (2011) observed a 200-m-thick nepheloid layer energized by ~60 extreme resuspension events each lunar cycle, where the waves suspend and redistribute bottom sediment (fine to medium sands, or a grain size of 0.125–0.5 mm). Ma et al. (2016) observed ISWs obliquely shoaling onto the shelf west of Dongsha Atoll, with strong near-bed oscillatory currents (>0.8 m/s). Sand waves and short scour channels near the shelf break had reasonable correlations with the presence of ISWs and strong internal tide-induced currents.

2.2. Sediment Transport by ISWs

Published observations of sediment transport by ISWs may be grouped into five geographic regions. These include the South China Sea, Northwest Australian Coast, Mediterranean Sea, Barents Sea and Bering Sea. The observations from each of these regions are reviewed below.

2.2.1. South China Sea. Reeder et al. (2011) observed sand waves on the continental slope at depths of 160–600 m formed by episodic shoaling of extreme ISWs (>100-m amplitudes) during each lunar cycle. The dunes were intermittently interspersed with lengthy smooth areas and had amplitudes of ≤ 16 m and crest-to-crest wavelengths of ≤ 350 m. The absence/presence of dunes is thought to result from the occurrence of stable/unstable internal waveforms during shoaling. West of Dongsha Atoll, Ma et al. (2016) observed ISWs and internal tides to be responsible for sediment transport in a region of two types of sand waves. For a typical stratification, ISWs of depression change polarity to elevation waves during shoaling (at depths of 130 m to 150 m), creating coarse and well-sorted sediment in type-1 sand wave fields, suggesting formation by convergence of wave-induced oscillatory currents. Upslope sediment transport, during shoaling, leads to asymmetry and migration. At deeper sites (~180 m), with steeper bed-slopes and finer sediment, internal tides force transport in type-2 sand wave fields, with crests parallel to the isobaths. The coexistence of the two classes of sand waves suggested that internal tides intensify and modify the upslope transport of the sediment suspended by ISWs, whereas at deeper sites, ISWs may enhance sediment supply and sorting through episodic resuspension but not alter the long-term migration.

2.2.2. Northwest Australian Coast. In the Browse Basin, ~60-m ISWs (with currents 0.7 m/s at 255-m depth) were observed concurrently with fields of sand waves having a lateral extent of several kilometers, heights of ≤ 10 m, and crest-to-crest wavelengths of 210–400 m (Beldé et al. 2015). The sand waves generally occurred below 250 m in the vicinity of bottom relief topography or the upslope area around the shelf break, the topography locally modulating the flow velocity and providing accumulation shelter for sediments otherwise transported across the shelf. Sand wave formation required currents between 0.3 and 1.5 m/s and bed slopes between 0.55° and 0.63°. Sand waves are common along the Australian margin parallel to bathymetric contours (Heap & Harris 2008).

2.2.3. Mediterranean Sea. Ribó et al. (2016) observed large-scale, fine-grained sand waves on the Gulf of Valencia continental slope. They cover 450 km², extending from depths of ~250–850 m, with wavelengths of 500–1,000 m and wave heights of 2–50 m, decreasing downslope. The largest dunes were observed at depths where ~50-m Kelvin–Helmholtz billows overturn (van Haren et al. 2013), causing upslope migration. The billows are thought to be generated by internal wave shoaling, which modulates sediment deposition without causing active resuspension. Enhanced turbulence prevents dune development on the steeper downslope flanks. Droghei et al. (2016) argued that sand waves in the Messina Strait (depths of 200–300 m, wavelengths of 60–120 m, wave heights of 1.5–5 m, and lateral extent of 100–300 m) result from ISWs that produce bottom currents

(~ 0.5 m/s) capable of mobilizing sediments into sand waves (**Figure 5**). The asymmetric nature of the wave field and decrease in wave size with depth are thought to be caused by ISW refraction over a topographic mound. Pipeline exposure and burial patterns suggest a migration rate of 10^{-2} to 1 m per year (Santoro et al. 2002), with significant decadal changes in bed form (Santoro et al. 2004) from reworking and/or migration. The sand waves are characterized by coarse sediment (coarse sand to gravel) with high bottom velocities removing finer material (Sell et al. 1978).

2.2.4. Barents Sea. Bøe et al. (2015) observed sand waves on the upper continental slope covering 130 km^2 at depths of 475–800 m, where energetic, high-frequency internal wave packets are expected to shoal along the main pycnocline. The sand waves had amplitudes of ≤ 6 m and asymmetric profiles. Sand from lower on the slope was likely transported upslope to accumulate in the dune fields, with migration at 2.5 m per year. Bottom currents of ~ 1 m/s were measured in the sand wave fields.

2.2.5. Bering Sea. Karl et al. (1986) observed sand waves at the heads of four of five large submarine canyons that incise the northern continental margin of the Bering Sea at depths of 175–490 m. They average 5 m in height and 650 m in wavelength, with crests parallel to contours. The bed forms are speculated to result from internal wave-induced currents.

Turning point: the depth on the shelf at which approaching internal solitary waves change from waves of depression to waves of elevation

No-slip boundary condition: requirement that the fluid has zero velocity, relative to the boundary, at the sediment/water interface; yields shear near the boundary and viscous drag on motions outside the bottom boundary layer

3. THEORETICAL, EXPERIMENTAL AND NUMERICAL RESULTS

3.1. Instability Mechanisms

From a theoretical point of view, sediment resuspension due to ISWs has been historically examined as a problem in hydrodynamic stability. The difficulty with this approach is that unlike well-defined topics like stratified, parallel shear flow, the background state is both complex and evolving. ISWs are modeled theoretically as inviscid phenomena, and while viscous effects are not expected to lead to sudden changes, the wave will evolve over time. Despite these difficulties, considerable progress has been made in identifying mechanisms of instability.

We categorize mechanisms of ISW-BBL interaction that lead to sediment resuspension into those originating from ISWs of depression (Section 3.1.1), elevation (Section 3.1.2), and ISW interaction with topography (Section 3.1.3). For the typical oceanic density stratification, consisting of a thin upper mixed layer above a thicker benthic zone, ISWs are waves of depression (**Figure 4a**) that are generated offshore (Helffrich & Melville 2006, Jackson et al. 2012). They may interact slowly with a flat bottom or more quickly with local topography. When shoaling into shallower water, they form waves of elevation at the turning point (note the difference from the mathematical meaning of the term) that degenerate into boluses of dense water propagating upslope along the bed (e.g., Helffrich 1992, Shroyer et al. 2009, Wallace & Wilkinson 1988).

3.1.1. ISWs of depression. Observations on the Palos Verdes shelf, California (Bogucki et al. 1997), reported resuspension by ISWs of depression in the presence of a background current, and early simulations (Bogucki & Redekopp 1999) suggested that a wave must contain a trapped core to incite resuspension. Diamessis & Redekopp (2006) revisited the issue using large-amplitude waveforms described by the approximate Korteweg–de Vries (KdV) equation; only waves of depression were considered (see the sidebar titled Korteweg–de Vries Weakly Nonlinear Theory). While it is well known that at large amplitude, the waves predicted by the KdV equation are too narrow, the basic mechanism proposed by Diamessis & Redekopp is believed to hold. Due to the no-slip boundary condition at the bottom, the large-scale, ISW-induced pressure gradients are not precisely balanced in the BBL, resulting in a jet oriented in the direction of propagation (i.e.,

KORTEWEG-DE VRIES WEAKLY NONLINEAR THEORY

KdV theory expands the stratified Euler equations in terms of two small parameters: a nondimensional amplitude (a/H) and an aspect ratio (H/L). Here H is the total depth, a is the dimensional wave amplitude, and L is a typical horizontal length scale. Assuming rightward propagation, the solution at first order is given by the KdV equation for the horizontal ISW structure,

$$A_t + cA_x + \alpha AA_x + \beta A_{xxx} = 0$$

and a Sturm–Liouville eigenvalue problem for the vertical structure and propagation speed, c . The nonlinearity (α) and dispersion (β) coefficients of the KdV equation are given by integral expressions involving the solutions of the eigenvalue problem (e.g., Helfrich & Melville 2006). The KdV equation admits exact solitary wave solutions, as well as a formal solution of the initial value problem using the so-called inverse scattering transform. However, the solitary wave solutions of the KdV equation are not solitary wave solutions of the full stratified Euler equations. Hence, the KdV equation is often referred to as a model equation that captures the qualitative physics of solitary wave formation and propagation but not its quantitative details. Higher-order extensions of the KdV equation are available in the literature but are largely of applied mathematical, as opposed to practical, interest.

a prograde jet) that trails the wave. When strong enough, this jet undergoes a shear instability. Diamessis & Redekopp (2006) argued that the instability of the jet is global in the sense that the instability continues to propagate with the ISW [see Chomaz (2005) and Briggs (1964) for a formal discussion]. This contrasts with a so-called convective instability that would fall behind the ISW. The possibility of a global instability is somewhat surprising since the stratified shear instabilities described in linear theory (i.e., by the Taylor–Goldstein equation) have propagation speeds that are much lower than the long wave speed, which in turn provides a strict lower bound on the ISW propagation speed. Recent developments in hydrodynamic stability adopt a simple background flow as a model ISW (e.g., Sumer et al. 2010) and increase the sophistication of the analysis, for example, using nonmodal stability theory. Verschaeve et al. (2018) found two different types of instability mechanisms, one of which is three-dimensional (3D), whose relative efficacy changes depending on the Reynolds number.

The theoretical predictions of Diamessis & Redekopp (2006) were confirmed in a qualitative sense by the experimental work of Carr & Davies (2006) and Carr et al. (2008). The experiments did not include an active sediment layer, but instability in the BBL including a trailing jet and clear vortices were observed. Similar jets have been observed in field observations (up to 8 m above the bed) (Bogucki et al. 1997). While these theoretical/numerical, experimental, and observational results are in qualitative agreement, quantitative comparisons of the critical Reynolds number revealed significant discrepancies between the methodologies (Aghsaei et al. 2012, Carr et al. 2008). Reasons for the differences include the disparity between KdV waves and waveforms generated in the experimental tank (Carr et al. 2008); differences between 3D and 2D instabilities in the direct numerical simulations (DNS) (Aghsaei et al. 2012); the lack of finite-amplitude perturbations in the numerical solution (Stefanakis 2010); and the existence of a gate-generated, oscillatory background barotropic flow in the laboratory, which may influence vortex generation (M. Carr, personal communication). The general scenario leading to resuspension is presented schematically in **Figure 6a**, with a clear suggestion of its efficacy in the field provided by **Figure 4a**. The spatially varying structure of the BBL currents is shown in **Figure 6c**.

Convective instability: a type of hydrodynamic instability occurring in stably stratified shear flows in which the growing disturbance is convected away from the site where it was generated

Global instability: a type of hydrodynamic instability in which the disturbance in a stably stratified shear flow grows at the generation site; also called absolute instability

Direct numerical simulation (DNS): a simulation that resolves all scales from those that force motion to those at which viscous dissipation occurs

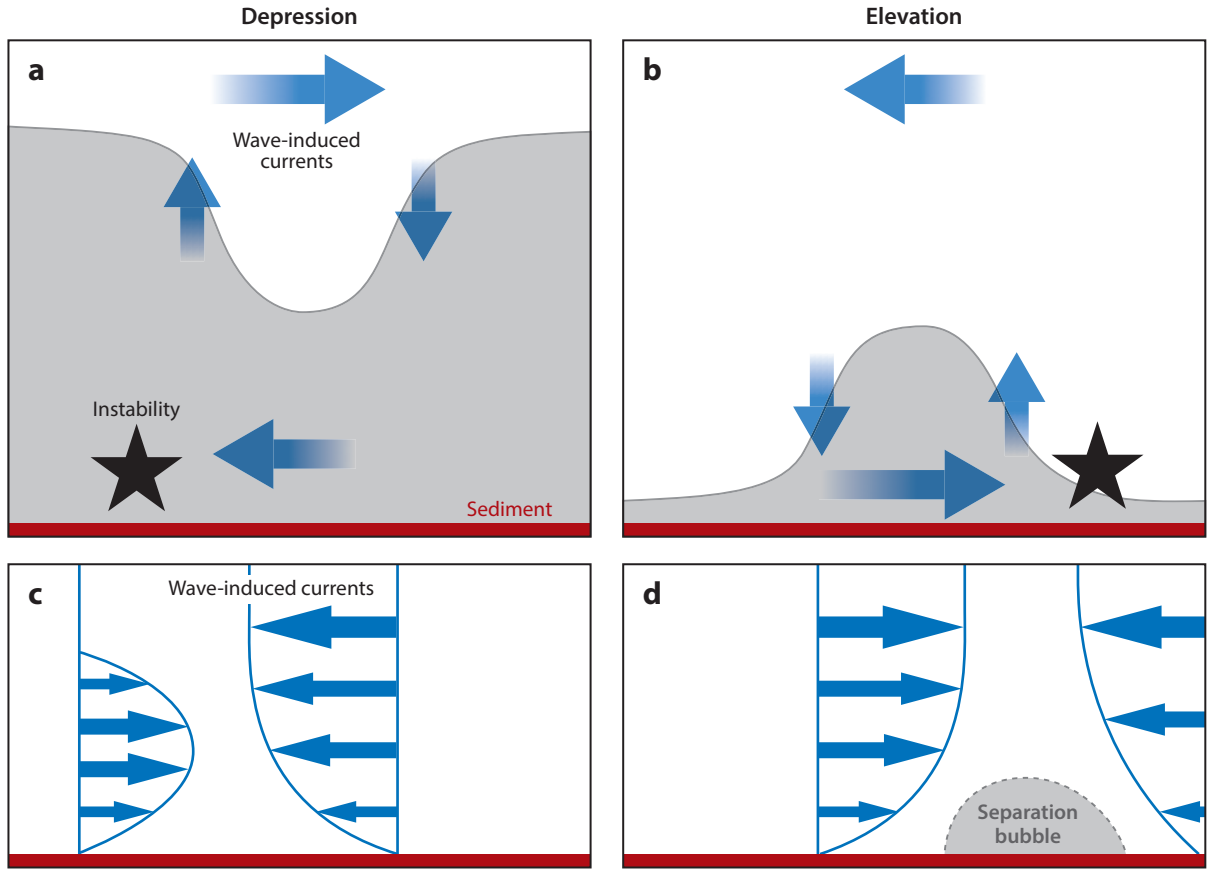


Figure 6

Instability mechanisms for internal solitary waves (ISWs) over a flat bottom. (a) The basic instability scenario for an ISW of depression propagating left to right. (b) The basic instability scenario for an ISW of elevation propagating left to right. A leftward-oriented background current is necessary for instability to occur. (c) Detail of the currents in the bottom boundary layer (BBL) for the ISW of depression case. (d) Detail of the currents in the BBL for the ISW of elevation case. For animations of instability mechanisms, the reader is referred to **Supplemental Videos 1–4**.

3.1.2. ISWs of elevation. ISWs of elevation were considered by Stastna & Lamb (2008). A global instability occurred near the front of the wave when a background current, oriented against the direction of wave propagation, was present and took the form of vortices ejected from the BBL up into the main water column (presented schematically in **Figure 6b**). When a background current was not present, an instability was not observed in either simulation or experiment (Carr & Davies 2010). While no observational visualization similar to **Figure 4a** has appeared in the literature, the measurements of Bogucki et al. (1997) appear to correspond to this scenario, and Moum et al. (2007, figure 9) reported a near-bottom peak in turbulent dissipation at the front of their shoaling wave of elevation. The spatially varying structure of the BBL currents, along with a forming separation bubble, is presented schematically in **Figure 6d**. Stastna & Lamb (2008) also demonstrated that the proposed scenario for waves of elevation occurs naturally during resonant generation of ISWs by flow over topography. Soontiens et al. (2015) reexamined the issue of BBL instability during resonant generation, finding significant differences between instability

Supplemental Material >

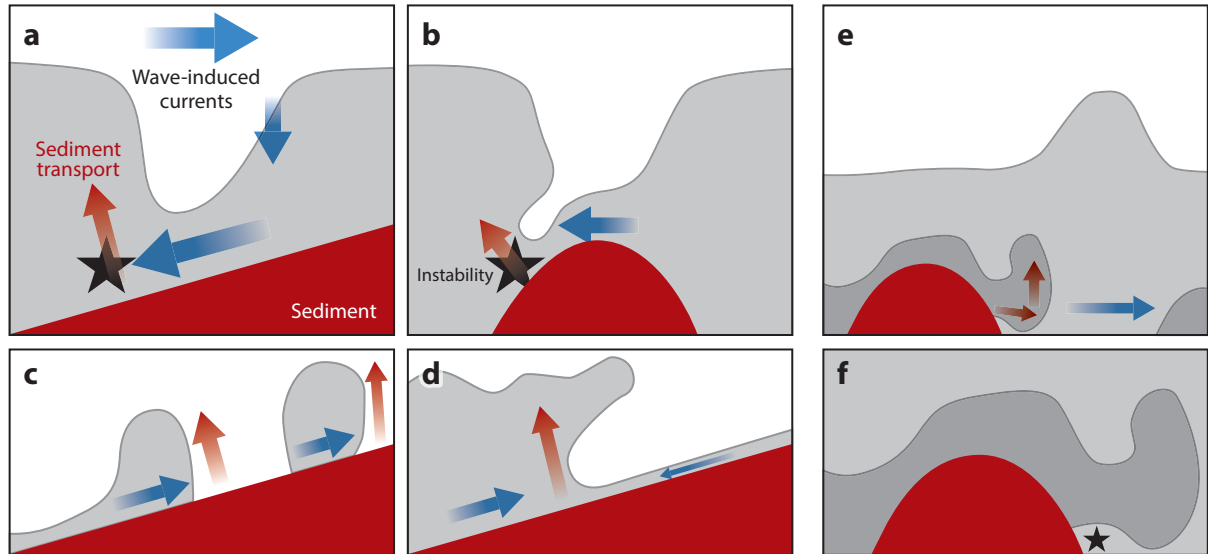


Figure 7

Schematic showing instability mechanisms for shoaling internal solitary waves (ISWs). The gray (white) color denotes the dense (light) fluid in a nearly two-layer stratification. (a) The instability scenario for a shoaling ISW of depression propagating left to right. (b) Instability and transport during passage of a wave of depression over large-amplitude, isolated topography. (c) Systematic transport from the bottom boundary layer (BBL) by upslope-propagating boluses. (d) Systematic transport from the BBL during downslope slumping (collapsing breaker). (e) Instability and transport during passage of a wave of elevation over isolated topography when near-bottom stratification is present. (f) Detail of panel e showing the location of Rayleigh–Taylor instability. Systematic transport of sediment from the BBL into the main water column is indicated by red gradient arrows in all panels. For animations of instability mechanisms, the reader is referred to **Supplemental Videos 1–4**.

Supplemental Material >

onset during wave generation over hill-type and trough-type topographies. For the hill-type case, instability was observed on both the upstream and downstream flanks, which is directly analogous to the scenarios for ISWs of elevation and depression. They also discussed the difficulties of Reynolds number scaling (Section 4).

3.1.3. ISW interaction with topography. ISW shoaling focuses wave energy, creating strong near-bottom currents. The ISW of depression also becomes asymmetric, with a steeper rear face. Both focusing and asymmetry imply that the adverse pressure gradient in the BBL becomes stronger. Thus, during shoaling an ISW of depression whose wave-induced currents are not vigorous enough to induce resuspension in the deep may reach the point on the bed at which instability is triggered (as shown in **Figure 7a**). Numerical simulations by Aghsaei et al. (2012, figure 5) provide a visualization.

As the ISW reaches the so-called turning point, the polarity changes from a wave of depression to a wave train of elevation waves (Lamb & Xiao 2014, Orr & Mignerey 2003, Shroyer et al. 2009). The expression of the complex dynamics in the BBL during the change of polarity remains comparatively unexplored in the published literature. Eventually, the waves reach the region in which the pycnocline intersects the sloping boundary. Here, the drawdown of the pycnocline and subsequent generation of upslope-propagating boluses have the potential to induce BBL turbulence and resuspension (**Figure 7c**). The effect of surface wave-induced currents is nonnegligible in this region (e.g., Wijesekera et al. 2013), but this effect remains unexplored in simulations. Boluses have been modeled by several authors, with 3D simulations by Arthur & Fringer (2014) providing

Rayleigh–Taylor instability:

the hydrodynamic instability that occurs when more dense fluid overlies less dense fluid

characterizations of mixing and Lagrangian transport. Laboratory experiments show boluses also result from convective ISW breaking (Boegman & Ivey 2009). Hosegood & van Haren (2004) observed convergence at the leading edge of boluses (solibores), with upward vertical velocities of ~ 10 cm/s, implying that they are the dominant cross-shelf sediment transport mechanism despite their intermittent occurrence. Moum et al. (2007) noted that wintertime stratification on the Oregon shelf favors the formation of near-bottom trains of elevation waves with significant near-bottom vertical currents that may transport resuspended material tens of meters above the bottom.

Since boluses transport denser water up the slope, the final phase of shoaling (presented schematically in **Figure 7d**) consists of a thin stratified jet of dense water directed downslope adjacent to the boundary. This jet may yield shear instability and BBL turbulence, as well as a larger overturning region where the jet meets the waves that are just beginning to shoal. Simulations of this final phase of evolution are extremely challenging because the prior phases, which are expected to be turbulent, must also be well represented. Moreover, typical slopes in the field are mild (Section 4), implying that the simulation domain must cover a large geographic area.

When the total depth is not changing monotonically, two further instability mechanisms have been identified (**Figure 7b,e,f**). For waves of depression, there is a weak instability of the prograde jet trailing the ISW (Harnanan et al. 2015). The mechanism is commonly known in the engineering literature as the Coanda effect (Newman 1961). However, the resulting currents do not appear to be strong enough to trigger sediment resuspension, at least on a laboratory scale. Using a coupled hydrodynamic/sediment model, Olsthoorn & Stastna (2014) reported that resuspension, in this circumstance, exhibited no spanwise variation. In contrast, sediment deposition was significantly 3D. A more vigorous instability occurs when the topography significantly modifies the waveform, leading to the ejection of light fluid from the wave (**Figure 7b**). The fluid accelerates below this lump of light fluid, leading to BBL separation, instability, and transport out of the BBL (**Figure 7b**). This mechanism was clearly identified in a combined experimental/simulation study on mode-2 wave propagation over isolated topography (Deepwell et al. 2017).

Finally, for ISWs of elevation, the presence of isolated topography and a stratification that includes near-bottom variation [e.g., observations in Monterey Bay by Cheriton et al. (2014b)] yields gravity current-like structures that trail the ISW as it passes over the topography (Harnanan et al. 2015), as presented schematically in **Figure 7ef**. This has been termed local hydraulics by Carr et al. (2010), in a combined experimental/simulation study of ISW propagation over bottom corrugations. The gravity current head is responsible for the majority of the three-dimensionalization, including coherent vortices. A smaller-scale Rayleigh–Taylor instability occurs in the region where the gravity current transports denser fluid across the topographic crest in the direction of wave propagation (**Figure 7f**).

3.2. Parameterizations and Their Experimental Tests

Sediment resuspension has historically been parameterized according to the viscous bed-shearing stress (e.g., Shields diagram). By fitting observed velocity profiles to the log law, Quaresma et al. (2007) modeled resuspension of sediments from ISWs of depression, with the Shields parameter exceeding critical mobility and resuspension levels during the passage of the leading wave, when acoustic backscatter showed strong resuspension (**Figure 4a**). However, in other studies, correlations between viscous bed stress and resuspension were not as clear. Bogucki et al. (1997) observed that resuspension coincides with periods of low bed shear stress, whereas Hosegood & van Haren (2004) and Moum et al. (2007) found vertical sediment fluxes during periods of high bed stress. Johnson et al. (2001) observed near-bottom optical attenuation spikes that coincided

with bottom-convergent currents at the trailing edge of the ISW and hence were not correlated with high bottom stress. They argued [as did Bogucki et al. (1997)] that bottom convergence must be associated with vertical motions that lift sediments off the bottom.

In the experiments by Boegman & Ivey (2009), elevated bed stress, without resuspension, was observed during the drawdown phase before breaking, as the ISW shoaled, suggesting that exceeding a critical bottom stress alone is not sufficient to induce resuspension; however, coherent vortices and turbulent bursts during ISW breaking were able to lift bed sediment (**Figure 2**). Oceanic observations (Bluteau et al. 2016) confirm that quadratic stress alone is insufficient to predict resuspension and enhanced turbulent kinetic energy is required. Aghsaei & Boegman (2015) modeled bed stress and experimentally visualized sediment resuspension from ISWs over a flat bottom. They showed that resuspension did not occur when bed stress was maximal, beneath the wave trough (**Figure 8c**), but rather when bursts of vertical velocity (**Figure 8d**) in the unstable separated-flow region lifted the bed sediment (**Figure 8a,b**).

A traditional Shields model did not predict resuspension, but rather a modified form was developed with the bed stress replaced by the maximum vertical bursting velocity (e.g., van Rijn 1993),

$$\tau_{\text{ISW}} = \rho w_{\max}^2, \quad 1.$$

where ρ is the fluid density at the bed. This model assumes the root-mean-square of w_{\max} is greater than the particle settling velocity, to lift sediments, and scales with the bottom shear velocity. Bluteau et al. (2016) showed that Equation 1 has better temporal agreement than the quadratic stress law with suspended sediment observations on the Tasman eastern continental shelf. From Equation 1, Aghsaei et al. (2012) parameterized resuspension to occur when the ISW-based Shields-type criterion,

$$\theta_{\text{ISW}} = \frac{\tau_{\text{ISW}}}{(\rho_s - \rho) gd_{50}} = \frac{\rho c_o^2 [0.09 \ln (Re_{\text{ISW}}) - 0.44]}{(\rho_s - \rho) gd_{50}} \gtrsim 0.7, \quad 2.$$

was achieved. Here, c_o is the linear phase speed, ρ_s is the sediment density, and d_{50} is the median grain size. To allow prediction of ISW-induced resuspension from only a thermistor mooring and knowledge of the sediment characteristics, Aghsaei et al. (2012) derived a parameterized momentum thickness Reynolds number as

$$Re_{\text{ISW}} = U \sqrt{L_w / [v(U + c)]},$$

where L_w is the characteristic half-wavelength (Michallet & Ivey 1999), c is the ISW phase speed, and U is the maximum ISW-induced near-bed horizontal velocity, which may be measured with a current profiler or estimated from the bulk wave properties (Ostrovsky & Stepanyants 2005). Manes & Brocchini (2015, equation 2.3) theoretically formalized the interaction between turbulent eddies and sediment, arguing that the bed stress is

$$\tau \sim \rho V^2 (d_{50}/S)^{1/3},$$

where V and S are, respectively, the characteristic length and velocity scales of the large eddies. Experimental observations of interfacial hydrodynamics show that sediment permeability controls when turbulent stresses dominate the bed stress (Voermans et al. 2017).

3.3. Field-Scale Simulations

The simulations and experiments discussed above fall into the category of process studies. This means that compared to field conditions, they isolate key physical processes. While the belief is

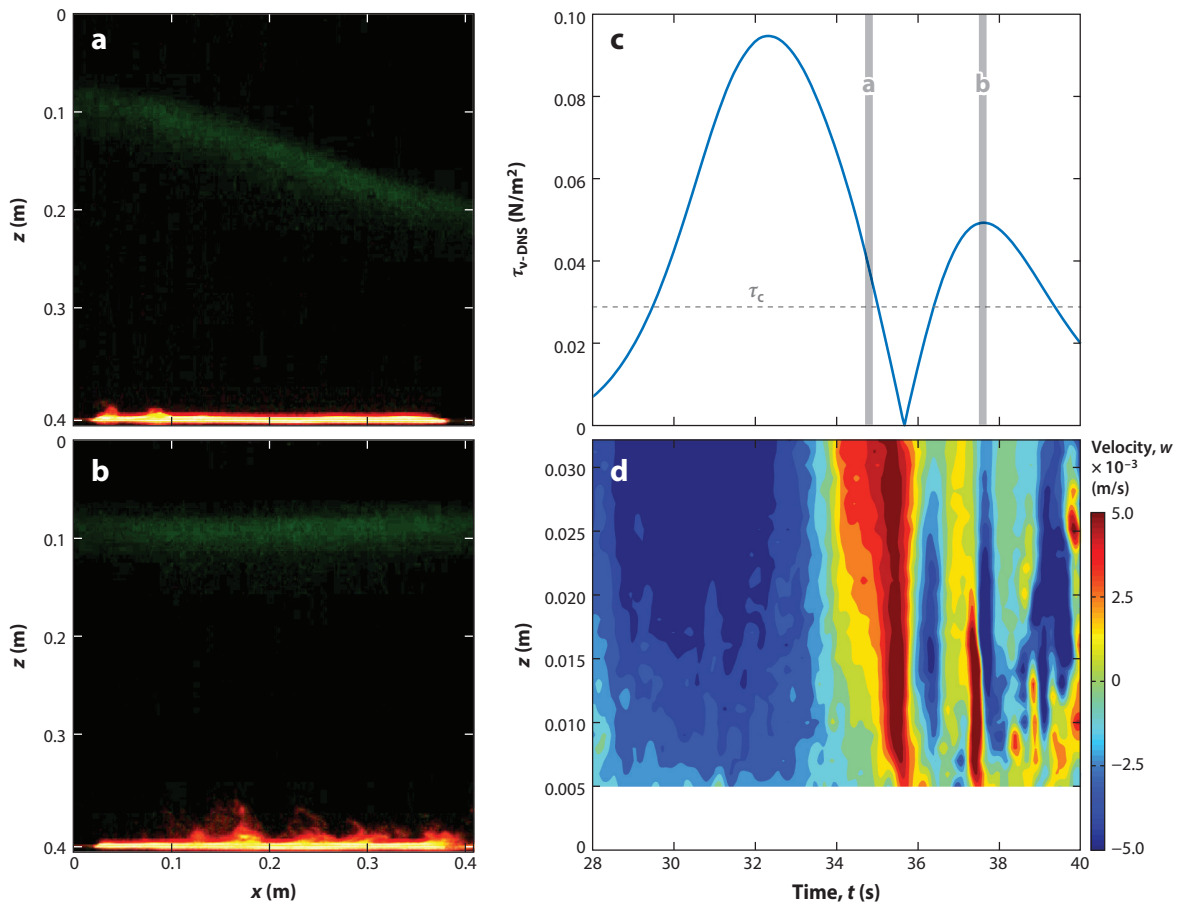


Figure 8

Experiments showing resuspension from internal solitary waves (ISWs) propagating from left to right over a flat bottom. (a,b) True-color bed sediment response showing the pycnocline in green (fluorescein) and the sediments in orange (rhodamine). (a) The initiation of resuspension. The near-bed jet propagates to the right through the region of resuspension in panels a and b. (b) Sediment resuspension within the unstable jet 2.7 s after the response shown in panel a. (c) Absolute value of direct numerical simulation (DNS)-modeled viscous bed stress. (d) Profiling acoustic Doppler velocimeter–observed instantaneous vertical velocity field. The gray dotted line in panel c gives the critical Shields stress for resuspension. Vertical gray lines in panel c show characteristic times associated with video images in panels a and b, but note that panels a and b and panels c and d are from different experimental runs. Figure generated using data from Aghsaei & Boegman (2015). For an animation of this experiment, the reader is referred to **Supplemental Videos 1–4**.

that the same mechanisms apply at the field scale, four key differences in the field are multiple scales of bottom topography, the larger-scale disparity between ISW and dissipative Kolmogorov scales (Aghsaei et al. 2010, figure 21), the presence of barotropic tides and baroclinic tides that may energize the BBL, and the often oblique propagation of ISWs relative to the bathymetric contours (Quaresma et al. 2007, figure 2). ISWs with trapped turbulent cores (Scotti & Pineda 2004), analogous to the upslope-propagating boluses shown in **Figure 7b**, provide an example of scale-up issues. This is because laboratory-scale studies (Luzzatto-Fegiz & Helffrich 2014) report that trapped cores are largely quiescent, albeit with enhanced turbulence due to convective overturns during shoaling (Wallace & Wilkinson 1988). A fully turbulent core/bolus may trigger different instabilities in the BBL (Scotti & Pineda 2004, figure 2) (see **Figures 3** and **4b**).

Barotropic tide:
oscillatory motion that is in phase across the entire water column and driven by lunar and solar gravitational forces

Baroclinic tide:

oscillatory motion that has vertical structure owing to vertical density stratification; an internal wave forced by the barotropic tide flowing over bottom topography

Reynolds-averaged Navier-Stokes (RANS) equation:

a RANS simulation yields a solution for the ensemble average but not an individual realization; a subgrid-scale closure model is required to account for the effects of Reynolds stresses on conservation of mean momentum

Reynolds stress:

the mean momentum transfer by the fluctuating velocity in a turbulent flow

Harnanan et al. (2015) suggested that 2D simulations, which resolve BBL dynamics and transition, are possible at the scale of a lake of moderate depth, but 3D simulations are impossible for any reasonable domain size (Botelho & Imberger 2007, Dorostkar et al. 2017, Scalo et al. 2013), and definitely not at oceanic scales (Section 4). This implies that other methods must be used when simulating sediment resuspension in the ocean. Bourgault et al. (2014) simulated resuspension during internal wave shoaling motivated by observations in the St. Lawrence estuary, using a laterally averaged Reynolds-averaged Navier-Stokes (RANS) equation model described in Bourgault & Kelley (2004). The BBL was parameterized via a quadratic stress law ($\tau \sim \rho U^2$), with an advection diffusion equation that includes settling for the sediment concentration. At the bottom boundary, sediment flux was given by a piecewise linear function of the bottom stress scaled by a critical value of shear stress. Using their numerical model, the authors produced images similar to acoustic backscatter images and were able to model significant nepheloid layers. Simulations of this type cannot represent the global instability (Section 3.1), especially over flat bottoms, and the resulting eddy dynamics over the bottom 10–50% of the water column, as reported by experiments (Aghsaei & Boegman 2015, Carr et al. 2008) and field measurements (Quaresma et al. 2007).

Masunaga et al. (2017) employed a version of the SUNTANS (Stanford unstructured non-hydrostatic terrain-following adaptive Navier-Stokes simulator) model (Fringer et al. 2006) to simulate the generation of nepheloid layers. The model employed the Mellor Yamada turbulence closure scheme, and the BBL was represented by the quadratic stress law. Erosion from the bottom was modeled by an exponential law written in terms of the excess stress (larger than the critical stress). They were able to generate nepheloid layers thought to represent field conditions and they observed dynamics consistent with smaller-scale DNS (Arthur & Fringer 2016).

Models similar to the two discussed above qualitatively capture the occurrence but not necessarily the exact timing of strong resuspension events (e.g., Lin et al. 2016). Bluteau et al. (2016, figure 3) observed on the Tasman eastern continental shelf that as the quadratic stress peaks, the flow laminarizes. Resuspension occurs only as the quadratic stress abates and near-bed turbulent kinetic energy increases. This is analogous to the resuspension dynamics beneath ISWs in the laboratory (Figure 8). Thus, the quadratic stress law cannot accurately predict all types of internal wave-induced resuspension. The more successful parameterization of Aghsaei & Boegman (2015), discussed above, used vertical velocities that may not be accurately represented in a RANS field-scale model employing quadratic stress (Bluteau et al. 2016). Hence, a more complete parameterization, perhaps making use of modeled subgrid-scale turbulence, remains a challenge for the future.

3.4. Laboratory Experiments on ISW-Induced Resuspension

Laboratory experiments are useful for visualization and idealized investigation of ISW-sediment interaction. Mixing associated with ISW breaking (Michallet & Ivey 1999), the breaking mechanism (Boegman et al. 2005a, Sutherland et al. 2013), and the location and upslope propagation of the breaker and/or bolus (Helffrich 1992, Wallace & Wilkinson 1988) have been investigated. Experiments by Southard & Cacchione (1972) on the breaking of interfacial waves over a planar slope with acrylic sediments showed that the waves broke abruptly as they shoaled, producing a turbulent bore that moved sediment upslope, partly in suspension, and downslope by the compensating return flow, as bed load (e.g., Figure 7d). Flow at the bed and net sediment transport were downslope. Boegman & Ivey (2009) visualized ISW breaking on a planar slope and found resuspension to occur where the flow separated from the bed, creating a spanwise vortex (Figure 2). The vortex applied a local bottom stress to mobilize sediment and provided a vertical lifting motion to resuspend bed material (Section 3.2), correlating resuspension with elevated instantaneous Reynolds stress at the bed (Figure 2c). After resuspension, the breaking ISW degenerated into

a turbulent bore that propagated upslope. On a flat bed, Aghsaei & Boegman (2015) observed mobile dunes with wisps of sediment lifting off the crests (**Figure 8a,b**) and a wavelength similar to the eddy size within the unstable region (Carr et al. 2008). Neither sediment ejection high into the water column (e.g., Moum et al. 2007) nor vertically migrating eddies (e.g., Aghsaei et al. 2012, Diamessis & Redekopp 2006) were observed (perhaps due to incorrect sediment scaling or 3D effects, respectively). The nascent wisps may lead to the formation of sand waves through interaction with eddies (Carr et al. 2010).

Southard & Cacchione (1972) found that the zone of sediment movement lies upslope of the point of breaking, which marks the transition from an undisturbed to a rippled bed. The band of sediment movement was more than an order of magnitude greater than the wave amplitude and was expected to vary with slope angle. Violent resuspension above the breaking point caused initial multidirectional sediment movement (as reported by Boegman & Ivey 2009) and then downslope bed load, which constructed ripples. Net downslope transport was at its maximum between the breaking point and the undisturbed bed above the breaker zone; deposition occurred in a narrow band just above the breaking point with erosion farther upslope. Fine sediment was resuspended and transported along isopycnals off slope (as in Bourgault et al. 2014). These laboratory results are strikingly consistent with the observations by Ma et al. (2016). Although experiments may guide first-order sediment transport dynamics, direct application to the ocean must be done with caution (Section 4).

3.5. Sediment Transport and Nepheloid Layer Formation

ISW shoaling can generate both bottom and intermediate nepheloid layers, with horizontal length scales ranging from hundreds of meters (St. Lawrence River estuary; Bourgault et al. 2014) to tens of kilometers [Oregon shelf (Moum et al. 2007) and the South China Sea (Reeder et al. 2011)]. From observations in the Faeroe–Shetland Channel, Hosegood & van Haren (2004) proposed that convergent currents in the ISW BBL induce vertical motions that resuspend sediment (as in Bogucki et al. 1997, Johnson et al. 2001). Boluses then transport the suspension upslope (Klymak & Moum 2003, Lamb 2002, Moum et al. 2007), with larger particles settling and finer particles (mud) being transported offshore with the return flow (Nakayama et al. 2012, Pomar et al. 2012) in an intrusive intermediate layer of mixed fluid (e.g., Ivey & Nokes 1989, McPhee-Shaw 2006). Qualitatively similar results were observed from echograms in the St. Lawrence River estuary (Bourgault et al. 2014, Richards et al. 2013) 30 min after ISW shoaling, although researchers were unable to verify that strong backscatter through the pycnocline originated as sediment (e.g., versus turbulence or zooplankton).

ISW-induced bottom nepheloid layers are typically ~10 m thick [the Portuguese mid-shelf (Quaresma et al. 2007), the Oregon shelf (Moum et al. 2007), and the St. Lawrence River estuary (Bourgault et al. 2014)] but may be significantly thicker in energetic environments. Reeder et al. (2011) argued that in the absence of any other mechanism, an ~200-m-thick nepheloid layer is the result of sediment resuspension induced by extremely large South China Sea transbasin ISWs. Two-dimensional RANS simulations (Bourgault et al. 2014) and field data (Moum et al. 2007) show that high bottom stress during shoaling, strong near-bottom vertical velocities, and boluses combine to generate a thick (~10–50 m) and sediment-rich bottom nepheloid layer, relative to the thin nepheloid layer (~1 m) during ISW propagation over a flat bottom.

3.6. Sand Wave Formation

Sand waves are believed to form in the convergence zones of the oscillatory current field beneath ISWs as they change polarity while shoaling (type 1) (Ma et al. 2016). Upslope sediment transport beneath bolus-like waves of elevation (e.g., Klymak & Moum 2003, Richards et al. 2013) leads

to sand wave asymmetry and upslope migration. This is supported by the Pomar et al. (2012) argument that hummocky-like cross-stratification sedimentary structures most likely result from ISW shoaling. These form in water deeper than the zone of ISW breakers, where the bottom is subjected to wave-induced oscillatory flows and a backwash return flow transports bed load and resuspension. These theories differ subtly, with Ma et al. (2016) arguing that sand wave formation occurs during the turning point transition and subsequent upslope bolus propagation, and Pomar et al. (2012) suggesting that formation occurs earlier in the shoaling process or on steeper slopes beneath ISWs of depression.

Laboratory observations by Southard & Cacchione (1972) support the Ma et al. (2016) theory, showing the transition from an undisturbed to a rippled bed occurring at the breaking point, with downslope bed features unrelated to wave action. Sand waves (with wavelengths of ~ 4 cm) scaled with the breaker vortex ($5\text{--}10$ cm) and were much smaller than the wave's typical length (~ 1 m). Sand waves were symmetrical immediately after the passage of the breaker and asymmetrical during downslope return flow. Solving conservation of mass, Southard & Cacchione showed rapid net deposition just upslope of the breaking and slower net erosion higher on the slope. On flat bottoms, Aghsaei & Boegman (2015) observed nascent dunes forming between the vortices in the unstable wake of a shoaling ISW of depression (dune wavelength similar to vortex diameter). Coupling between the ISW and bed-corrugation wavelength can amplify vortex formation and presumably sand wave growth (Carr & Davies 2010). Although this vortex-generation mechanism is not a direct result of wave-induced oscillatory currents, it may occur prior to the turning point in deeper water (as in Pomar et al. 2012). Scale effects for wave-dune interaction in the laboratory, where $a/a_{\text{dune}} = \mathcal{O}(1)$, remain to be investigated, as this is not typical of the ocean, where the ISW amplitude a is on the order of 10–100 m and dune amplitude a_{dune} is on the order of 1–10 m (Carr et al. 2010).

Theoretical modeling of sand wave formation and migration does not explicitly include ISW effects. Development and application of sand wave models can be found in the literature (Droghei et al. 2016, Hulscher & Dohmen-Janssen 2005, Ma et al. 2016).

4. CONCLUSIONS AND FUTURE OUTLOOK

In general, the dynamics of ISW–sediment interaction remains speculative, without sufficient guiding theories, models, and laboratory data (Bourgault et al. 2014). This is coupled with a paucity of field observations, particularly those that measure bottom stress and sediment profiles through the water column (Section 2). Consequently, the turbulent wave-breakdown process, as these waves shoal, and the interactions with bed sediment in coastal regions remain poorly understood. The difficulties in conducting research on ISWs result from the multiscale 3D nature (from wavelengths of ~ 1 km to dissipative eddies of ~ 1 cm) of ISWs, which makes field observation challenging. Moreover, the large oceanic Reynolds numbers cannot be reproduced in the laboratory, and the waves are not resolved in the typically applied computational lake and coastal ocean models. ISWs are nonhydrostatic features that require high-resolution grids and small time steps, making accurate simulation of these waves a challenge, both at laboratory scale (i.e., DNS) and field scale (i.e., RANS). Simply put, we lack the laboratory facilities and computational power to reproduce ISWs and their 3D interactions with sediments at the level of field-relevant Reynolds numbers. Computationally intensive RANS simulations can reproduce 3D ISW evolution (10^8 grid cells on 90 CPUs for 7 months) (Dorostkar et al. 2017) and associated billowing (Barad & Fringer 2010, Botelho & Imberger 2007) in lake-sized domains, but in ocean models with larger domains, ISWs are often underresolved (e.g., Zhang et al. 2011). Flow separation along the bottom boundary during breaking was found to be a process that controls the breaking mechanism, and consequently

the vertical grid-point resolution must not only resolve the wave amplitude but also be sufficient to capture the no-slip boundary condition (Aghsaei et al. 2010).

Many field-scale numerical simulations of internal wave shoaling do not have sufficient vertical grid resolution (Δz) to resolve the BBL [for example, $\Delta z = 0.53$ m (Lamb 2002), $\Delta z = 3.3$ m (Legg & Adcroft 2003), $\Delta z = 0.5$ m (Bourgault & Kelley 2003), and $\Delta z = 6$ m (Vlasenko & Stashchuk 2007)]. These values are larger than the boundary layer thickness and thus these simulations (some of which did not use a no-slip bottom boundary condition and hence were also missing some essential physics) were not capable of capturing the flow separation processes central to regulation of the breaking mechanism. For example, the 2D field-scale simulations by Vlasenko & Hutter (2002, figure 6) used a no-slip bottom boundary condition with $\Delta z = 0.5$ m to simulate plunging breakers associated with a Rayleigh–Taylor instability; however, flow separation was not simulated to occur as is expected in a plunging breaker, likely due to coarse grid resolution (see the sidebar titled Classification of ISW Breaking Regimes).

To increase vertical resolution, researchers often employ 2D simulations; however, these miss some essential physics of wave breaking (Aghsaei et al. 2012, figure 13) and associated turbulence (Fringer & Street 2003, figure 30). As an alternative, vertically varying resolution has been effectively applied to resolve BBL beneath ISWs (Diamessis & Redekopp 2006, Stastna & Lamb 2008) at low-wave Reynolds numbers ($Re_w \sim 10^4$). Here, we define $Re_w \sim a c_o / v$, where we typically have $Re_w \sim 10^3$ in the laboratory and $\sim 10^6 < Re_w < \sim 10^7$ in lakes and oceans. Upon shoaling, an $\mathcal{O}(10)$ decrease in Re_w (10^4 versus 10^3) results in a thicker BBL, relative to the wave amplitude, with larger shed vortices that have faster growth rates and impede plunging of the wave face, modifying both the separation and breaker mechanisms (Aghsaei et al. 2010, figure 21) (see the sidebar titled Classification of ISW Breaking Regimes). Similarly, DNS for a case with Re_w reduced by a factor of 4 from $\sim 10^5$ showed a much different evolution of BBL instabilities (Soontiens et al. 2015).

While DNS provide much richer flow field data relative to experiments, to finally allow meaningful comparisons, one needs to address numerical simulations' long-standing inability (since Carr et al. 2008) to directly reproduce experimental observations. DNS of ISW shoaling at field-relevant $Re_w \sim (0.1 \text{ m/s})(10 \text{ m})/(10^{-6} \text{ m}^2/\text{s}) \sim 10^6$ would require 10^{13} grid points and 10^4 Tb of memory, which is projected to be computationally intractable for at least the next several decades (Fringer 2009). Wall-resolved large-eddy simulations (reviewed in Sarkar & Scotti 2017) remain a presently feasible (10^8 grid cells on 512 CPUs for two weeks; Fringer 2009) but underexplored approach to investigate ISW shoaling and resuspension.

Laboratory experiments on ISW dynamics also remain problematic. Southard & Cacchione (1972) noted that experiments do not represent a true scale model of the ocean because sediment size is too large relative to the waves, and due to the low value of Re_w , the length scale disparity between the wave scale and the Kolmogorov scale is unrealistically small (Aghsaei et al. 2010, figure 21). In the laboratory, $Re_w \sim 10^3$ is limited by the flume depth ($a < \sim 1$ m) and viscosity ($v \sim 10^{-6} \text{ m}^2/\text{s}$), leaving c_o as the only option to raise Re_w through the addition of salt to the lower fluid layer (to a practical maximum value of $\sim 1,100 \text{ kg/m}^3$; Aghsaei & Boegman 2015). The laboratory-scale Re_w is significantly smaller than oceanic values, $Re_w \sim 10^7$, which are not achievable, leading to scale effects.

To model ISW–sediment interactions in the laboratory, one should scale sediment grain size with the length scales characterizing the ISW, leading to noncohesive oceanic sediments (e.g., sand) being scaled to cohesive laboratory sediment (e.g., silt) unless the oceanic sediments have grain sizes greater than 2 mm (nearly gravel). As a result, realistic sediment modeling in the laboratory is not possible; the bed form patterns in the model and field are not properly reproduced (Kamphuis 2010). Ideally, both Froude and Reynolds numbers would be matched between the ocean and laboratory to maintain dynamic similarity for both gravity-driven (waves and currents)

Large-eddy simulation:

a simulation that resolves a significant portion of the energy-containing scales and inertial subrange but does not aim to resolve the scales of viscous dissipation (with energy removal modeled via an eddy viscosity)

and viscosity-related (BBL and sediment transport) processes. However, this cannot be achieved due to the inability to adjust gravity and viscosity concurrently with length and velocity scaling (Kamphuis 2010).

Given the present laboratory and numerical challenges associated with process-oriented investigation of ISW shoaling, resuspension, and sediment transport at field-relevant Reynolds numbers, there is a need to support continued field observations on this topic. Direct oceanographic observations of sediment resuspension by ISWs remain sparse (Section 2) in comparison to observed ISW generation sites (**Figure 1**). Hence, oceanographers require parameterizations to infer sediment resuspension from ISWs, using readily measured-modeled wave parameters (J. Moum, personal communication) to more easily predict wave-induced resuspension from mooring data. However, initial attempts to derive such parameterizations have been unsuccessful, likely due to scale effects, flume roughness, and/or inconsistent dimensional analysis (Aghsaei & Boegman 2015, Aghsaei et al. 2012, Carr et al. 2008, Diamessis & Redekopp 2006).

Most wave shoaling events (e.g., Oregon shelf, New Jersey shelf, South China Sea) occur on mild slopes ($0.001 < S < 0.01$; Baines 2008, Moum 2012) where fission is the predominant breakdown process as solitary waves change polarity from waves of depression to elevation during shoaling (Aghsaei et al. 2010, Lamb & Xiao 2014, Shroyer et al. 2009). However, process studies on ISW-induced resuspension have only been undertaken on steep slopes [$S = 0.1$ (Southard & Cacchione 1972); $S = 0.145$ (Boegman & Ivey 2009)], hill/small-bank topography (Olsthoorn & Stastna 2014), and flat bottoms (Aghsaei & Boegman 2015). There is a need for sediment-related, process-based research on mild slopes (e.g., following Helffrich 1992, Wallace & Wilkinson 1988) to parameterize and quantify the upslope and offshore mass transport as a function of grain size and wave/boundary slope, the latter of which regulates the breaking mechanism (Aghsaei et al. 2010, Boegman et al. 2005a, Sutherland et al. 2013). This research will advance our understanding of coastal sediment processes and help improve our ability to model sediment dynamics, resuspension, and transport on the continental shelf.

RANS simulations at field scale have shown ISW shoaling to be an effective mechanism for offshore dispersal of muddy sediments (Bourgault et al. 2014). However, it remains unclear when sediment is transported upslope, along with a bolus (turbulent bore) from a shoaling ISW, or offshore in a mixed-fluid intrusion. Observations show boluses to have elevated sediment concentrations (Carter et al. 2005, Klymak & Moum 2003, Moum et al. 2007, Richards et al. 2013, Scotti & Pineda 2004), whereas RANS models predict the opposite (Bourgault et al. 2014). This discrepancy may be due to boluses transporting large particles upslope, while fine particles are advected offshore in intrusions. Present numerical approaches, limited to a single sediment type and quadratic stress law, have been unable to investigate such nepheloid dynamics (Bourgault et al. 2014).

Finally, there is a need for research to support the oil and gas industry (Jones & Ivey 2017). Migration of sand waves leads to pipeline exposure and burial, although wavelength and migration rate may be reasonably predicted (Nemeth et al. 2003). Poor understanding of BBL turbulence and sediment movement beneath ISWs, however, results in conservative design conditions, such as secondary stabilization and overengineering of pipeline wall thickness. Better constraining load criteria for design could potentially save tens of millions of dollars per development (G. Wake, personal communication).

SUMMARY POINTS

1. Internal solitary waves (ISWs) have been observed on nearly every coastline worldwide, but few field campaigns have investigated ISW-induced sediment resuspension and transport.

2. Shoreward-propagating ISWs of depression are generated offshore from tide-topography interaction. They may interact slowly with a flat bottom or more quickly with local topography. When shoaling into shallower water, they form waves of elevation at the turning point that degenerate into bulges of dense water propagating upslope along the bed.
3. Near-bed global instability, along with associated vertical burst-type currents, is believed to be the principal mechanism driving ISW-induced sediment resuspension.
4. ISWs become unstable through interaction with the bottom boundary. Due to the no-slip boundary condition at the bed, the large-scale, ISW-induced pressure gradients are not precisely balanced in the bottom boundary layer, resulting in a prograde jet that trails the wave. When strong enough, this jet undergoes an instability.
5. ISW shoaling can generate both bottom and intermediate nepheloid layers that are tens to hundreds of meters thick, with horizontal length scales ranging from hundreds of meters to tens of kilometers. Mixing and resuspension from ISW shoaling are thought to be sufficient to supply the required nutrients to the euphotic zone in coastal regions.
6. To date, DNS have not been able to reproduce laboratory experiments of ISW shoaling. Reynolds-averaged Navier–Stokes (RANS) equation simulations are commonly under-resolved and remain unable to capture the no-slip bottom boundary condition.
7. The mechanisms behind ISW–sediment interaction remain speculative. Our knowledge of ISW-induced resuspension is limited by the paucity of field observations, scale effects from low Reynolds numbers employed in the laboratory, the lack of computational power for simulations, and poor parameterizations for both RANS modeling and analysis of field data.
8. There is a need for more process-oriented research on ISW shoaling and resuspension on mild slopes ($0.001 < S < 0.01$), which are common to coastal regions yet remain underinvestigated in the laboratory and numerically. This will advance our understanding of coastal sediment processes and help improve our ability to model sediment dynamics, resuspension, and transport on the continental shelf.

DISCLOSURE STATEMENT

The authors are not aware of any biases that might be perceived as affecting the objectivity of this review.

ACKNOWLEDGMENTS

We thank Bruce Sutherland, Greg Ivey and Kevin Lamb for providing detailed comments on a draft version of this manuscript. Discussions with Peter Diamessis and Magda Carr are gratefully acknowledged, as is the work of all graduate students who contributed to the papers discussed above.

LITERATURE CITED

Aghsaei P, Boegman L. 2015. Experimental investigation of sediment resuspension beneath internal solitary waves of depression. *J. Geophys. Res. Oceans* 120:3301–14

- Aghsaei P, Boegman L, Diamessis PJ, Lamb KG. 2012. Boundary-layer-separation-driven vortex shedding beneath internal solitary waves of depression. *J. Fluid Mech.* 690:321–44
- Aghsaei P, Boegman L, Lamb KG. 2010. Breaking of shoaling internal solitary waves. *J. Fluid Mech.* 659:289–317
- Arthur RS, Fringer OB. 2014. The dynamics of breaking internal solitary waves on slopes. *J. Fluid Mech.* 761:360–98
- Arthur RS, Fringer OB. 2016. Transport by breaking internal gravity waves on slopes. *J. Fluid Mech.* 789:93–126
- Baines PG. 2008. Mixing in downslope flows in the ocean-plumes versus gravity currents. *Atmos. Ocean* 46:405–19
- Barad MF, Fringer OB. 2010. Simulations of shear instabilities in interfacial gravity waves. *J. Fluid Mech.* 644:61–95
- Barth JA, Lerezak JA, Calantoni J, Chickadel CC, Colosi JA, et al. 2018. *An overview of the 2017 Point Sal, California, Inner Shelf Dynamics experiment*. Paper presented at the 2018 Ocean Sciences Meeting, Portland, OR, Feb. 11–16
- Belde J, Back S, Reuning L, Eberli G. 2015. Three-dimensional seismic analysis of sediment waves and related geomorphological features on a carbonate shelf exposed to large amplitude internal waves, Browse Basin region, Australia. *Sedimentology* 62:87–109
- Bluteau CE, Smith S-L, Ivey GN, Schlosser TL, Jones NL. 2016. *Assessing the relationship between bed shear stress estimates and observations of sediment resuspension in the ocean*. Paper presented at 20th Australasian Fluid Mechanics Conference, Dec. 5–8. <https://people.eng.unimelb.edu.au/imarusic/proceedings/20/473%20Paper.pdf>
- Bøe R, Skarðhamar J, Rise L, Dolan MFJ, Bellec VK, et al. 2015. Sandwaves and sand transport on the Barents Sea continental slope offshore northern Norway. *Mar. Petroleum Geol.* 60:34–53
- Boegman L, Imberger J, Ivey GN, Antenucci JP. 2003. High-frequency internal waves in large stratified lakes. *Limnol. Oceanogr.* 48:895–919
- Boegman L, Ivey GN. 2009. Flow separation and resuspension beneath shoaling nonlinear internal waves. *J. Geophys. Res. Oceans* 114:C02018
- Boegman L, Ivey GN, Imberger J. 2005a. The degeneration of internal waves in lakes with sloping topography. *Limnol. Oceanogr.* 50:1620–37
- Boegman L, Ivey GN, Imberger J. 2005b. The energetics of large-scale internal wave degeneration in lakes. *J. Fluid Mech.* 531:159–180
- Bogucki D, Dickey T, Redekopp LG. 1997. Sediment resuspension and mixing by resonantly generated internal solitary waves. *J. Phys. Oceanogr.* 27:1181–96
- Bogucki DJ, Redekopp LG. 1999. A mechanism for sediment resuspension by internal solitary waves. *Geophys. Res. Lett.* 26:1317–20
- Bogucki DJ, Redekopp LG, Barth J. 2005. Internal solitary waves in the Coastal Mixing and Optics 1996 experiment: multimodal structure and resuspension. *J. Geophys. Res. Oceans* 110:C02024
- Bonnin J, van Haren H, Hosegood P, Brummer G-JA. 2006. Burst resuspension of seabed material at the foot of the continental slope in the Rockall Channel. *Mar. Geol.* 226:167–84
- Botelho DA, Imberger J. 2007. Downscaling model resolution to illuminate the internal wave field in a small stratified lake. *J. Hydraul. Eng.* 133:1206–18
- Bourgault D, Kelley DE. 2003. Wave-induced boundary mixing in a partially mixed estuary. *J. Mar. Res.* 61:553–76
- Bourgault D, Kelley DE. 2004. A laterally averaged nonhydrostatic ocean model. *J. Atmos. Ocean. Technol.* 21:1910–24
- Bourgault D, Morsilli M, Richards C, Neumeier U, Kelley DE. 2014. Sediment resuspension and nepheloid layers induced by long internal solitary waves shoaling orthogonally on uniform slopes. *Cont. Shelf Res.* 72:21–33
- Briggs RJ. 1964. *Electron-Stream Interaction with Plasmas*. Cambridge, MA: MIT Press
- Butman B, Alexander PS, Scotti A, Beardsley RC, Anderson SP. 2006. Large internal waves in Massachusetts Bay transport sediments offshore. *Cont. Shelf Res.* 26:2029–49

- Cacchione DA, Pratson LF, Ogston AS. 2002. The shaping of continental slopes by internal tides. *Science* 296:724–27
- Carr M, Davies PA. 2006. The motion of an internal solitary wave of depression over a fixed bottom boundary in a shallow, two-layer fluid. *Phys. Fluids* 18:016601
- Carr M, Davies PA. 2010. Boundary layer flow beneath an internal solitary wave of elevation. *Phys. Fluids* 22:026601
- Carr M, Davies PA, Shivaram P. 2008. Experimental evidence of internal solitary wave-induced global instability in shallow water benthic boundary layers. *Phys. Fluids* 20:066603
- Carr M, Stastna M, Davies PA. 2010. Internal solitary wave-induced flow over a corrugated bed. *Ocean Dyn.* 60:1007–25
- Carter GS, Gregg MC, Lien R-C. 2005. Internal waves, solitary-like waves, and mixing on the Monterey Bay shelf. *Cont. Shelf Res.* 25:1499–520
- Chang M-H, Lien R-C, Tang TY, D’Asaro EA, Yang YJ. 2006. Energy flux of nonlinear internal waves in northern South China Sea. *Geophys. Res. Lett.* 33:L03607
- Cheriton OM, McPhee-Shaw EE, Shaw WJ, Stanton TP, Bellingham JG, Storlazzi CD. 2014a. Suspended particulate layers and internal waves over the southern Monterey Bay continental shelf: An important control on shelf mud belts? *J. Geophys. Res. Oceans* 119:428–44
- Cheriton OM, McPhee-Shaw EE, Storlazzi CD, Rosenberger KJ, Shaw WJ, Raanan BY. 2014b. Upwelling rebound, ephemeral secondary pycnoclines, and the creation of a near-bottom wave guide over the Monterey Bay continental shelf. *Geophys. Res. Lett.* 41:8503–11
- Chomaz J-M. 2005. Global instabilities in spatially developing flows: non-normality and nonlinearity. *Annu. Rev. Fluid Mech.* 37:357–92
- Deepwell D, Stastna M, Carr M, Davies PA. 2017. Interaction of a mode-2 internal solitary wave with narrow isolated topography. *Phys. Fluids* 29:076601
- Diamessis PJ, Redekopp LG. 2006. Numerical investigation of solitary internal wave-induced global instability in shallow water benthic boundary layers. *J. Phys. Oceanogr.* 36:784–812
- Dorostkar A, Boegman L, Pollard A. 2017. Three-dimensional simulation of high-frequency nonlinear internal wave dynamics in Cayuga Lake. *J. Geophys. Res. Oceans* 122:2183–204
- Droghei R, Falcini F, Casalbore D, Martorelli E, Mosetti R, et al. 2016. The role of internal solitary waves on deep-water sedimentary processes: the case of up-slope migrating sediment waves off the Messina Strait. *Sci. Rep.* 6:36376
- Farmer DM. 1978. Observations of long nonlinear internal waves in a lake. *J. Phys. Oceanogr.* 8:63–73
- Fringer OB. 2009. Towards nonhydrostatic ocean modeling with large-eddy simulation. *Oceanography* 2025:81–83
- Fringer OB, Gerritsen M, Street R. 2006. An unstructured-grid, finite-volume, nonhydrostatic, parallel coastal ocean simulator. *Ocean Model.* 14:139–73
- Fringer OB, Street RL. 2003. The dynamics of breaking progressive interfacial waves. *J. Fluid Mech.* 494:319–53
- Fructus D, Carr M, Grue J, Jensen A, Davies PA. 2009. Shear-induced breaking of large internal solitary waves. *J. Fluid Mech.* 620:1–29
- Harnanan S, Soontiens N, Stastna M. 2015. Internal wave boundary layer interaction: a novel instability over broad topography. *Phys. Fluids* 27:016605
- Haury LR, Briscoe MG, Orr MH. 1979. Tidally generated internal wave packets in Massachusetts Bay. *Nature* 278:312
- Heap A, Harris P. 2008. Geomorphology of the Australian margin and adjacent seafloor. *Aust. J. Earth Sci.* 55:555–85
- Helffrich C. 1992. Internal solitary wave breaking and run-up on a uniform slope. *J. Fluid Mech.* 243:133–54
- Helffrich KR, Melville WK. 2006. Long nonlinear internal waves. *Annu. Rev. Fluid Mech.* 38:395–425
- Hosegood P, Bonnin J, van Haren H. 2004. Solibore-induced sediment resuspension in the Faeroe-Shetland Channel. *Geophys. Res. Lett.* 31:L09301
- Hosegood P, van Haren H. 2004. Near-bed solibores over the continental slope in the Faeroe-Shetland Channel. *Deep Sea Res. II* 51:2943–71

- Huang X, Chen Z, Zhao W, Zhang Z, Zhou C, et al. 2016. An extreme internal solitary wave event observed in the northern South China Sea. *Sci. Rep.* 6:30041
- Hulscher SJMH, Dohmen-Janssen CM. 2005. Introduction to special section on marine sand wave and river dune dynamics. *J. Geophys. Res. Earth Surf.* 110:F04S01
- Ivey G, Nokes R. 1989. Vertical mixing due to the breaking of critical internal waves on sloping boundaries. *J. Fluid Mech.* 204:479–500
- Jackson C. 2007. Internal wave detection using the Moderate Resolution Imaging Spectroradiometer (MODIS). *J. Geophys. Res.* 112:C11012
- Jackson CR, Da Silva JC, Jeans G. 2012. The generation of nonlinear internal waves. *Oceanography* 25:108–23
- Johnson DR, Weidemann A, Pegau WS. 2001. Internal tidal bores and bottom nepheloid layers. *Cont. Shelf Res.* 21:1473–84
- Jones NL, Ivey GN. 2017. Internal waves. In *Encyclopedia of Maritime and Offshore Engineering*, ed. PJ Carlton, YW Choo. Hoboken, NJ: Wiley. <https://doi.org/10.1002/9781118476406.emoe089>
- Kamphuis JW. 2010. *Introduction to Coastal Engineering and Management*. Singapore: World Sci. 2nd ed.
- Karl H, Cacchione D, Carlson P. 1986. Internal-wave currents as a mechanism to account for large sand waves in Navarinsky Canyon head, Bering Sea. *J. Sediment. Res.* 56:706–14
- Klymak JM, Moum JN. 2003. Internal solitary waves of elevation advancing on a shoaling shelf. *Geophys. Res. Lett.* 30(20):2045
- Lamb KG. 2002. A numerical investigation of solitary internal waves with trapped cores formed via shoaling. *J. Fluid Mech.* 451:109–44
- Lamb KG. 2014. Internal wave breaking and dissipation mechanisms on the continental slope/shelf. *Annu. Rev. Fluid Mech.* 46:231–54
- Lamb KG, Xiao W. 2014. Internal solitary waves shoaling onto a shelf: comparisons of weakly-nonlinear and fully nonlinear models for hyperbolic-tangent stratifications. *Ocean Model.* 78:17–34
- Legg S, Adcroft A. 2003. Internal wave breaking at concave and convex continental slopes. *J. Geophys. Oceanogr.* 33:2224–46
- Lien RC. 2005. Energy of nonlinear internal waves in the South China Sea. *Geophys. Res. Lett.* 32:L05615
- Lin SQ, Valipour R, Zhao YM, Boegman L. 2016. *Sediment resuspension modeling in Lake Erie*. Paper presented at the 59th Annual Conference on Great Lakes Research, Guelph, Ont., June 6–10
- Luzzatto-Fegiz P, Helffrich KR. 2014. Laboratory experiments and simulations for solitary internal waves with trapped cores. *J. Fluid Mech.* 757:354–80
- Ma X, Yan J, Hou Y, Lin F, Zheng X. 2016. Footprints of obliquely incident internal solitary waves and internal tides near the shelf break in the northern South China Sea. *J. Geophys. Res. Oceans* 121:8706–19
- Manes C, Brocchini M. 2015. Local scour around structures and the phenomenology of turbulence. *J. Fluid Mech.* 779:309–24
- Masunaga E, Arthur RS, Fringer OB, Yamazaki H. 2017. Sediment resuspension and the generation of intermediate nepheloid layers by shoaling internal bores. *J. Mar. Syst.* 170:31–41
- McPhee-Shaw E. 2006. Boundary–interior exchange: reviewing the idea that internal-wave mixing enhances lateral dispersal near continental margins. *Deep Sea Res. II* 53:42–59
- Meiburg E, Kneller B. 2010. Turbidity currents and their deposits. *Annu. Rev. Fluid Mech.* 42:135–56
- Michallet H, Ivey G. 1999. Experiments on mixing due to internal solitary waves breaking on uniform slopes. *J. Geophys. Res. Oceans* 104:13467–77
- Moum JN. 2012. *Advances in oceanic nonlinear internal waves: highlights of the new millennium*. Paper presented at the 2012 Ocean Sciences Meeting, Salt Lake City, UT, Feb. 20–24
- Moum JN, Farmer DM, Smyth WD, Armi L, Vagle S, et al. 2003. Structure and generation of turbulence at interfaces strained by internal solitary waves propagating shoreward over the continental shelf. *J. Geophys. Oceanogr.* 33:2093–112
- Moum JN, Klymak JM, Nash JD, Perlin A, Smyth WD. 2007. Energy transport by nonlinear internal waves. *J. Geophys. Oceanogr.* 37:1968–88
- Nakayama K, Shintani T, Kokubo K, Kakinuma T, Maruya Y, et al. 2012. Residual currents over a uniform slope due to breaking of internal waves in a two-layer system. *J. Geophys. Res. Oceans* 117:C10002
- Nash JD, Moum JN. 2005. River plumes as a source of large-amplitude internal waves in the coastal ocean. *Nature* 437:400

- Nemeth A, Hulscher SJ, de Vriend HJ. 2003. Offshore sand wave dynamics, engineering problems and future solutions. *Pipeline Gas J.* 230:67–69
- Newman B. 1961. The deflection of plane jets by adjacent boundaries—Coanda effect. *Boundary Layer Flow Control*, Vol. 1, ed. GV Lachmann, pp. 232–64. New York: Pergamon
- Olsthoorn J, Stastna M. 2014. Numerical investigation of internal wave-induced sediment motion: resuspension versus entrainment. *Geophys. Res. Lett.* 41:2876–82
- Orr MH, Mignerey PC. 2003. Nonlinear internal waves in the South China Sea: observation of the conversion of depression internal waves to elevation internal waves. *J. Geophys. Res. Oceans* 108(C3):3064
- Ostrovsky L, Stepanyants YA. 2005. Internal solitons in laboratory experiments: comparison with theoretical models. *Chaos* 15:037111
- Pomar L, Morsilli M, Hallock P, Bádenas B. 2012. Internal waves, an under-explored source of turbulence events in the sedimentary record. *Earth-Sci. Rev.* 111:56–81
- Quaresma LS, Vitorino J, Oliveira A, da Silva J. 2007. Evidence of sediment resuspension by nonlinear internal waves on the western Portuguese mid-shelf. *Mar. Geol.* 246:123–43
- Rayson MD, Ivey GN, Jones NL, Meuleners MJ, Wake GW. 2011. Internal tide dynamics in a topographically complex region: Browse Basin, Australian North West Shelf. *J. Geophys. Res. Oceans* 116:C01016
- Rayson MD, Jones N, Ivey G. 2012. Temporal variability of the standing internal tide in the Browse Basin, Western Australia. *J. Geophys. Res. Oceans* 117:C06013
- Reeder DB, Ma BB, Yang YJ. 2011. Very large subaqueous sand dunes on the upper continental slope in the South China Sea generated by episodic, shoaling deep-water internal solitary waves. *Mar. Geol.* 279:12–18
- Ribó M, Puig P, Muñoz A, Lo Iacono C, Masqué P, et al. 2016. Morphobathymetric analysis of the large fine-grained sediment waves over the Gulf of Valencia continental slope (NW Mediterranean). *Geomorphology* 253:22–37
- Richards C, Bourgault D, Galbraith PS, Hay A, Kelley DE. 2013. Measurements of shoaling internal waves and turbulence in an estuary. *J. Geophys. Res. Oceans* 118:273–86
- Sandstrom H, Elliott JA. 1984. Internal tide and solitons on the Scotian Shelf: a nutrient pump at work. *J. Geophys. Res. Oceans* 89:6415–26
- Santoro VC, Amore E, Cavallaro L, Cozzo G, Foti E. 2002. Sand waves in the Messina Strait, Italy. *J. Coastal Res.* 36:640–53
- Santoro VC, Amore E, Cavallaro L, De Lauro M. 2004. Evolution of sand waves in the Messina Strait, Italy. *Ocean Dyn.* 54:392–98
- Sarkar S, Scotti A. 2017. From topographic internal gravity waves to turbulence. *Annu. Rev. Fluid Mech.* 49:195–220
- Scalo C, Boegman L, Piomelli U. 2013. Large-eddy simulation and low-order modeling of sediment-oxygen uptake in a transitional oscillatory flow. *J. Geophys. Res. Oceans* 118:1926–39
- Scotti A, Pineda J. 2004. Observation of very large and steep internal waves of elevation near the Massachusetts coast. *Geophys. Res. Lett.* 31:L22307
- Scotti A, Pineda J. 2007. Plankton accumulation and transport in propagating nonlinear internal fronts. *J. Mar. Res.* 65:117–45
- Sellì R, Colantoni P, Fabbri A, Rossi S, Borsetti A, Gallignani P. 1978. Marine geological investigation on the Messina Strait and its approaches. *G. Geol.* 42:1–70
- Shroyer EL, Moum JN, Nash JD. 2009. Observations of polarity reversal in shoaling nonlinear internal waves. *J. Geophys. Oceanogr.* 39:691–701
- Soontiens N, Stastna M, Waite ML. 2015. Topographically generated internal waves and boundary layer instabilities. *Phys. Fluids* 27:086602
- Southard JB, Cacchione DA. 1972. Experiments on bottom sediment movement by breaking internal waves. In *Shelf-Sediment Transport: Process and Pattern*, ed. DJP Swift, DB Duane, OH Pilkey, pp. 83–97. Stroudsburg, PA: Dowden, Hutchinson & Ross
- Stastna M, Lamb KG. 2008. Sediment resuspension mechanisms associated with internal waves in coastal waters. *J. Geophys. Res.* 113:C10016
- Stefanakis T. 2010. *Bottom boundary layer instabilities induced by nonlinear internal waves*. MSc Thesis, Cornell Univ., Ithaca, NY

- Sumer BM, Jensen PM, Sørensen LB, Fredsøe J, Liu PL-F, Carstensen S. 2010. Coherent structures in wave boundary layers. Part 2. Solitary motion. *J. Fluid Mech.* 646:207–31
- Sutherland BR, Barrett KJ, Ivey GN. 2013. Shoaling internal solitary waves. *J. Geophys. Res. Oceans* 118:4111–24
- Thorpe SA. 1971. Asymmetry of the internal seiche in Loch Ness. *Nature* 231:306
- Thorpe SA. 1998. Some dynamical effects of internal waves and the sloping sides of lakes. In *Physical Processes in Lakes and Oceans*, ed. J Imberger, pp. 441–60. Washington, DC: Am. Geophys. Union
- Valipour R, Boegman L, Bouffard D, Rao YR. 2017. Sediment resuspension mechanisms and their contributions to high-turbidity events in a large lake. *Limnol. Oceanogr.* 62:1045–65
- van Haren H, Ribó M, Puig P. 2013. (Sub-)inertial wave boundary turbulence in the Gulf of Valencia. *J. Geophys. Res. Oceans* 118:2067–73
- van Rijn LC. 1993. *Principles of Sediment Transport in Rivers, Estuaries and Coastal Seas*. Amsterdam: Aqua
- Verschaeve JC, Pedersen GK, Tropea C. 2018. Non-modal stability analysis of the boundary layer under solitary waves. *J. Fluid Mech.* 836:740–72
- Vlasenko V, Hutter K. 2002. Numerical experiments on the breaking of solitary internal waves over a slope–shelf topography. *J. Geophys. Oceanogr.* 32:1779–93
- Vlasenko V, Stashchuk N. 2007. Three-dimensional shoaling of large-amplitude internal waves. *J. Geophys. Res.* 112:C11018
- Voermans J, Ghisalberti M, Ivey G. 2017. The variation of flow and turbulence across the sediment–water interface. *J. Fluid Mech.* 824:413–37
- Wallace B, Wilkinson D. 1988. Run-up of internal waves on a gentle slope in a two-layered system. *J. Fluid Mech.* 191:419–42
- Wang YH, Dai CF, Chen YY. 2007. Physical and ecological processes of internal waves on an isolated reef ecosystem in the South China Sea. *Geophys. Res. Lett.* 34:L18609
- Wijesekera H, Wang D, Teague W, Jarosz E, Rogers W, et al. 2013. Surface wave effects on high-frequency currents over a shelf edge bank. *J. Geophys. Oceanogr.* 43:1627–47
- Zhang Z, Fringer OB, Ramp SR. 2011. Three-dimensional, nonhydrostatic numerical simulation of nonlinear internal wave generation and propagation in the South China Sea. *J. Geophys. Res.* 116:C05022